Posted on 7 Dec 2022 — CC-BY 4.0 — https://doi.org/10.1002/essoar.10512768.1 — This a preprint and has not been peer reviewed. Data may be preliminary.

High-resolution mantle flow models reveal importance of plate boundary geometry and slab pull forces on generating tectonic plate motions

Arushi Saxena[1], Juliane Dannberg[1], Rene Gassmöller[1], Menno Fraters[2], Timo Heister[3], and Richard H Styron[4]

[1]University of Florida
[2]University of California, Davis
[3]Clemson University
[4]Earth Analysis

December 7, 2022

Abstract

Mantle convection models based on geophysical constraints have provided us with a basic understanding of the forces driving and resisting plate motions on Earth. However, existing studies computing the balance of underlying forces are contradicting, and the impact of plate boundary geometry on surface deformation remains unknown. We address these issues by developing global instantaneous 3-D mantle convection models with a heterogeneous density and viscosity distribution and weak plate boundaries prescribed using different geometries. We find that the plate boundary geometry of the Global Earthquake Model (GEM, Pagani et al., 2018), featuring open plate boundaries with discrete lithospheric-depth weak zones in the oceans and distributed crustal faults within continents, achieves the best fit to the observed GPS data with a directional correlation of 95.1% and a global point-wise velocity residual of 1.87 cm/year. A good fit also requires plate boundaries being 3 to 4 orders of magnitude weaker than the surrounding lithosphere and low asthenospheric viscosities between 5e17 and 5e18 Pa s. Models without asthenospheric and lower mantle heterogeneities retain on average 30% and 70% of the plate speeds, respectively. Our results show that Earth's plate boundaries are not uniform and better described by more discrete plate boundaries within the oceans and distributed faults within continents. Furthermore, they emphasize the impact of plate boundary geometry on the direction and speed of plate motions and reaffirm the importance of slab pull in the uppermost mantle as a major plate driving force.

High-resolution mantle flow models reveal importance of plate boundary geometry and slab pull forces on generating tectonic plate motions

Arushi Saxena[1], Juliane Dannberg[1], Rene Gassmöller[1], Menno Fraters[2], Timo Heister[3], and Richard Styron[4]

[1]Department of Geological Sciences, University of Florida, Gainesville, FL, USA
[2]Department of Earth and Planetary Sciences, University of California, Davis, CA, USA
[3]Mathematical and Statistical Sciences, Clemson University, Clemson, SC, USA
[4]Global Earthquake Model Foundation, Pavia, Italy

Key Points:

- We model plate motions in global instantaneous 3-D mantle convection models with different plate boundary geometries
- Earth's plate boundaries are not uniform and better described by discrete shear zones in the oceans and distributed faults within continents
- Slab pull within the uppermost mantle (< 300 km depth) contributes about 70% of the total plate driving force

Corresponding author: Arushi Saxena, `saxena.arushi@ufl.edu`

Abstract

Mantle convection models based on geophysical constraints have provided us with a basic understanding of the forces driving and resisting plate motions on Earth. However, existing studies computing the balance of underlying forces are contradicting, and the impact of plate boundary geometry on surface deformation remains unknown. We address these issues by developing global instantaneous 3-D mantle convection models with a heterogeneous density and viscosity distribution and weak plate boundaries prescribed using different geometries. We find that the plate boundary geometry of the Global Earthquake Model (GEM, Pagani et al., 2018), featuring open plate boundaries with discrete lithospheric-depth weak zones in the oceans and distributed crustal faults within continents, achieves the best fit to the observed GPS data with a directional correlation of 95.1% and a global point-wise velocity residual of 1.87 cm/year. A good fit also requires plate boundaries being 3 to 4 orders of magnitude weaker than the surrounding lithosphere and low asthenospheric viscosities between 5×10^{17} and 5×10^{18} Pa s. Models without asthenospheric and lower mantle heterogeneities retain on average 30% and 70% of the plate speeds, respectively. Our results show that Earth's plate boundaries are not uniform and better described by more discrete plate boundaries within the oceans and distributed faults within continents. Furthermore, they emphasize the impact of plate boundary geometry on the direction and speed of plate motions and reaffirm the importance of slab pull in the uppermost mantle as a major plate driving force.

Plain Language Summary

Plate tectonics can explain several geological and geophysical phenomena on Earth and is closely coupled to convection in the underlying mantle. To understand this plate–mantle coupling and quantify the forces contributing to plate motion, we develop high-resolution three-dimensional computational models of the Earth's present-day mantle flow utilizing available geophysical constraints on density distribution and rheology. Additionally, we prescribe weak zones at the location of plate boundaries. We use different plate boundary geometries, forming either open or closed polygons, and we vary how easily the plate boundaries and the asthenosphere directly below the plates can be deformed to determine which model best fits observed plate motions. Our best-fitting model features open plate boundaries that are weak (∼4 order of magnitude weaker than the surrounding lithosphere) and traverse the whole plate in the oceans, but are shallower and more distributed within continents. The asthenosphere in these models is even weaker than the plate boundaries. Furthermore, we find that the downward force caused by subducted slabs contributes the most to the observed surface velocities. Our models suggest that plate boundaries are not uniformly weak everywhere and that their geometry has a strong influence on the direction and speed of plate motion.

1 Introduction

Plate tectonic forces shape some of the most remarkable geological features on Earth and without plate tectonics, complex life on Earth would not be possible. Therefore, tectonic forces have been studied extensively. With the increased availability of computational resources and advanced numerical techniques, mantle flow models based on observational constraints have become an increasingly common tool for investigating global tectonics and how the contributing plate-driving and resisting forces affect the motion of plates. These models usually derive their temperature distribution from a seismic tomography model, and in some cases additional data sets, and then use the corresponding buoyancy forces to predict global plate motions. For instance, Zhong (2001) studied the effects of plate–mantle coupling and the viscosity contrast between oceanic and continental plates on the observed surface plate motions and the geoid, infering the location of subducted slabs from the Earth's subduction history and using an upper-mantle structure from seismic tomography. To investigate the relative importance of slab pull and slab suction forces for the plate motions, Conrad and Lithgow-Bertelloni (2002) analyzed a model with slab geometries based on plate reconstructions. Becker (2006) studied how lateral viscosity variations computed from the SMEAN tomography model (Becker & Boschi, 2002) affect plate motions and Euler poles. In an advanced high-resolution global mantle convection model based on tomography and a slab database, Stadler et al. (2010) resolved plate boundaries at the $\sim$1 km-scale to fit the observed plate motions and plateness. Osei Tutu, Sobolev, et al. (2018) investigated the contribution of various plate-driving and resisting forces on the plate motions and Euler poles using mantle flow models based on a well-resolved uppermost mantle temperature distribution and the SMEAN tomographic model at depths >300 km. And Liu and King (2022) explored what drives the motion of the North American plate by varying the buoyancy forces associated with velocity anomalies in their tomography model.

All of these models highlight the importance of buoyancy forces from both the upper and the lower mantle for reproducing the observed surface deformation. However, there are substantial discrepancies between different studies regarding the relative contributions of the forces that drive plate motions. Conrad and Lithgow-Bertelloni (2002, 2004) find that slab pull in the upper mantle accounts for about 50% to 70% of the total plate driving force and the rest is accommodated by slab suction in the lower mantle, emphasizing the importance of upper mantle buoyancy. The models by Stadler et al. (2010) and Alisic et al. (2012) even show a better fit to the plate velocities if only slab pull in the upper mantle is considered and the lower mantle is assumed to be homogeneous compared models with lower-mantle heterogeneity. On the other hand, the models of Osei Tutu, Sobolev, et al. (2018) predict that 70% of the plate-driving force comes from lower mantle buoyancy alone.

This difference in model results also highlights that developing self-consistent global mantle flow models that reproduce the observed plate motions remains a challenging problem. The complexity of the problem arises from the interplay of numerous physical processes governing mantle flow at different time and length scales, and the associated necessity to incorporate physical properties of vastly different magnitudes from the Earth's surface to the core-mantle boundary into a single model (e.g., Schubert et al., 2001; Heister et al., 2017). The different scale of deformation at plate boundaries compared to convection cells in the mantle means that coupling these processes requires a high resolution and/or the use of an adaptive grid. This is associated with large computational costs. Non-linear rheologies and strong viscosity contrasts between plates and plate boundaries pose challenges for solving the governing equations numerically. Furthermore, the unknown present thermal and chemical state of the Earth imposes a limit on how well buoyancy forces can be constrained. To achieve the most accurate results, different types of models and observations (seismic tomography, heat flux, plate age, present and past locations of subduction zones, plate boundary geometry, etc.) need to be combined. Due to these challenges, the influence of various model components and the associated physical properties of the mantle on the observed surface deformation are still open questions, that we try to answer here.

The seismic tomography used as an input determines how well a model can resolve mantle buoyancy and therefore affects the modeled force balance controlling plate motions (Becker & O'Connell, 2001). A common choice in previous mantle convection models has been a degree-20 (S20RTS, Ritsema & Van Heijst, 2000) or degree-40 (S40RTS, Ritsema et al., 2011) shear-wave velocity model—used by Stadler et al. (2010); Liu and King (2022), or an averaged shear wave model, SMEAN (Becker & Boschi, 2002)—used in Becker (2006); Osei Tutu, Steinberger, et al. (2018). Since then, increased station coverage and advances in computational resources have made it possible to create tomography models that utilize both P-waves—that can better resolve the subducted slabs (e.g., Li et al., 2008; Simmons et al., 2012), and shear-waves—that can better resolve the low-velocity anomalies (e.g., Becker & Boschi, 2002). These more robust models can reach a resolution of 1 degree (Simmons et al., 2015, 2019), but their effect on the accuracy of the equivalent buoyant forces and the corresponding plate motions remain to be tested.

In order to generate plate-like motion, existing models use weak zones at locations corresponding to the Nuvel plate boundary model (DeMets et al., 1990). Since then, an updated plate boundary model by Bird (2003)—comprising of several micro-plates and regions of more complex deformation inside the plate boundary polygons—has been proposed. Additionally, in an effort to map the global seismic hazard, the Global Earthquake Model, consisting of over 13,000 active faults and their detailed geometry, has been made publicly available (Styron & Pagani, 2020). To date, global mantle flow models in the literature (e.g., Stadler et al., 2010; Osei Tutu, Steinberger, et al., 2018; Liu & King, 2022) have not studied the effects of different plate boundary geometries (other than Nuvel) on surface deformation and it remains unclear which plate boundary model best reproduces the observed plate motions.

Here, we address the questions raised above by developing global compressible mantle flow models based on a high-resolution seismic tomography that jointly inverts for P- and S-wave traveltimes, LLNL-G3D-JPS (Simmons et al., 2015), and four different plate boundary geometries. We investigate which of the components of a geodynamic model—and which corresponding force in the Earth's mantle—is most important to reproduce the Earth's present-day plate motions. In addition, we explore how different plate boundary geometry models affect the surface plate motions and their fit to observations. Based on the best-fitting model, we quantify the relative influence of the driving and resisting forces on the motion of the tectonic plates.

2 Methods

2.1 Governing equations

We use global 3D instantaneous models of mantle convection, solving the compressible Stokes equations in the following form:

$$-\nabla \cdot (2\eta\dot{\varepsilon}) + \nabla p = \rho\mathbf{g}, \tag{1}$$

$$\nabla \cdot (\rho\mathbf{u}) = 0, \tag{2}$$

where η is the shear viscosity, $\dot{\varepsilon}$ is the deviatoric strain rate, p is the pressure, ρ is the density, $\mathbf{g}$ is the gravitational acceleration, and $\mathbf{u}$ is the velocity. Since our models are instantaneous, we do do not solve equations for the conservation of energy or the tracking of materials. Therefore, the only material properties directly appearing in the equations are the density and viscosity. The density depends on pressure, temperature and composition (Section 2.4), and the viscosity depends on temperature, composition, depth, and strain-rate (Section 2.5). We note that we use the Anelastic Liquid Approximation (Jarvis & Mckenzie, 1980) to solve equation (2) so it is reformulated to:

$$\nabla \cdot (\rho_{\mathrm{ref}}\mathbf{u}) = 0, \tag{3}$$

where $\rho_{\mathrm{ref}}(z)$ is the depth-dependent reference profile. This is an improvement on previous studies (Osei Tutu, Steinberger, et al., 2018; Liu & King, 2022) that have assumed an incompressible mantle. To compute the reference profile, we use the density at the adiabatic pressure and temperature in the uppermost mantle (where temperatures are based on the TM1 model, see Section 2.3), and PREM below that.

Our model geometry is a three-dimensional spherical shell with an inner radius of 3481 km and an outer radius of 6371 km (and accordingly, a thickness of 2890 km). We

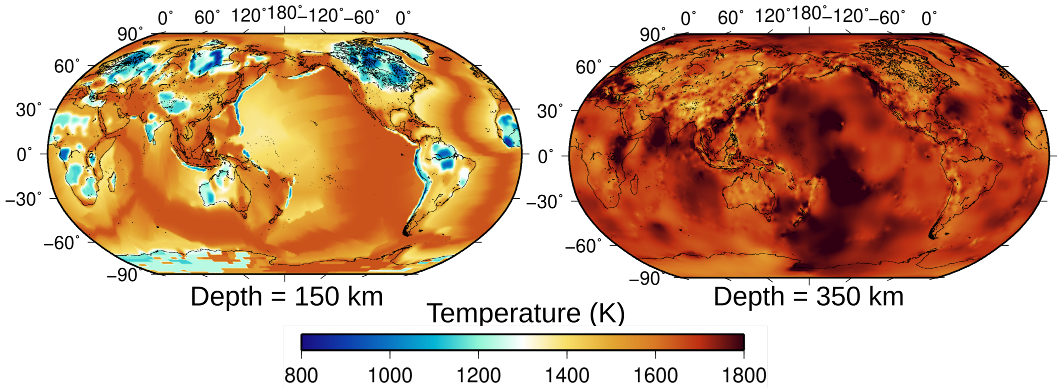

Figure 1. Temperature distribution at depth layers of 150 km (left) and 350 km (right) using the TM1 model (Osei Tutu, Sobolev, et al., 2018) and the LLNL-G3D-JPS tomography model (Simmons et al., 2015), respectively.

use free slip boundary conditions at both the top and bottom boundary, and remove the net rotation of the surface to constrain the resulting rotational degree of freedom. This allows us to compare modeled surface velocities to measured GPS velocities in a no-net-rotation reference frame.

2.2 Numerical methods

To solve Equations (1) and (2), we use the open-source geodynamic modeling software ASPECT (Kronbichler et al., 2012; Heister et al., 2017; Bangerth et al., 2022b), which has been successfully benchmarked for global spherical mantle flow computations (Liu & King, 2019). ASPECT is a finite-element modeling package that uses stable Taylor-Hood (Q2Q1) elements to discretize the Stokes system (velocity and pressure), and employs an iterative preconditioned GMRES solver to solve the resulting linear system.

For the Stoke system, we make use of the recently implemented matrix-free solver and geometric multigrid preconditioner (Clevenger & Heister, 2021), which scales efficiently up to 100,000 compute cores, and reduces ASPECT's memory requirements significantly. This allows us to run large-scale instantaneous models like the ones in this study on relatively few cores. A requirement of this solver is to cell-wise average the viscosity as defined in Section 2.5, and for our models we choose a harmonic average.

ASPECT makes use of the libraries deal.II (Arndt et al., 2021) and p4est (Burstedde et al., 2011) to discretize the geometry into 3D hexahedra that are organized into a hierarchical unstructured adaptive mesh stored as a forest of octrees. Each hexahedron utilizes a nonlinear fourth-order mapping from unit cell to real cell, which allows to account for the spherical curvature of each element. To be able to model thin plate boundaries, we utilize ASPECT's adaptive mesh and use a resolution between approximately 17 km and 82 km depending on the location in the model (see Figure 2, right panel). This range of resolutions results in models of approximately one billion degrees of freedom, with a typical graphical output size of 18 GB. Our models were run on 5376 cores at the NSF supercomputing system Frontera at TACC with smaller test models run on 512 cores at SDSC Expanse.

2.3 Initial temperature and composition

We infer the initial temperature in our model from published crust, lithosphere and subducted slab models (above 200 km depth) and global seismic tomography models (below 200 km depth). Figure 1 shows two depth slices of these two temperature models. In addition, the temperature is fixed to 273 K at the surface and to 3700 K at the core-mantle boundary.

In the top 200 km, we use the temperature distribution of the TM1 temperature model from Osei Tutu, Steinberger, et al. (2018). This model includes the thermal structure of continents based on their age from model TC1 (Artemieva, 2006), temperatures of oceanic plates computed using a half-space cooling model and plate ages from Müller et al. (2008), and vertical slabs using location and depth from Steinberger (2000).

For the rest of the model, we use the joint P- and S-wave 1°-tomography model LLNL-G3D-JPS by Simmons et al. (2015) and use a depth-dependent scaling factor to convert from S-wave velocity anomalies to temperature anomalies (Steinberger & Calderwood, 2006). We add these anomalies to a reference temperature profile based on a mantle adiabat with a potential temperature of 1573 K, which we chose to prevent jumps in the average mantle temperature at 200 km depth between the TM1 and LLNL-G3D-JPS models. To compute the adiabatic profile, we integrate downwards starting from the potential temperature at the surface, using the thermal expansivity profile from Steinberger and Calderwood (2006), a specific heat of 1200 J/kg/K, and the density profile from PREM.

We smooth the transition between the TM1 model above 200 km and the tomography-derived temperature below using a sigmoid function with a half-width of 20 km. This smooth transition avoids jumps in material properties in regions of the model where the temperature deviates from the reference adiabat (in regions where the temperature is equal to the adiabat, our choice of potential temperature guarantees continuity between the two models).

It may be surprising that we compute a temperature field at all, because the instantaneous Stokes equations do not contain the temperature itself. However, the density and viscosity in the Earth's mantle depend on temperature and composition and therefore we need these fields to compute the material properties in the Stokes equations.

We note that the depth of the transition between a temperature model based on lithosphere thickness and a seismic tomography model is a choice with potentially significant effects on the model results. Previous mantle convection studies (Conrad & Lithgow-Bertelloni, 2006; Becker, 2006; Osei Tutu, Steinberger, et al., 2018) have achieved good results using a transition depth of 300 km. Our choice of using the higher-resolution TM1 model only up to 200 km depth is based on several tests with varying transition depths (between 100 km and 300 km depth, see Table S1 for more details). In these models, a transition depth of 200 km achieved the best fit to observed plate velocities, which is likely caused by a particular assumption of the TM1 temperature model. TM1 introduces vertically dipping cold temperature anomalies at subduction zones to represent subducted slabs, while the fast anomalies in the tomography model obviously occur at the observed slab locations (with varying dip angles depending on the individual subduction zone). In other words, TM1 resolves the slab pull force from vertical slabs in the shallow sub-lithospheric mantle very well, but has the drawback that many slabs are disconnected from the dipping slabs in the tomography model if the model is used down to 300 km depth. Our chosen transition depth of 200 km is deep enough to accurately reflect the thickness of all oceanic and nearly all continental plates, since cold cratonic roots are represented in the seismic tomography model as well, and at the same time achieves a better connectivity of subducted slabs than a deeper transition. This model outcome again illustrates the importance of resolving slab pull forces and slab connectivity on global plate velocities (see also Zhong et al., 1998; Conrad et al., 2004).

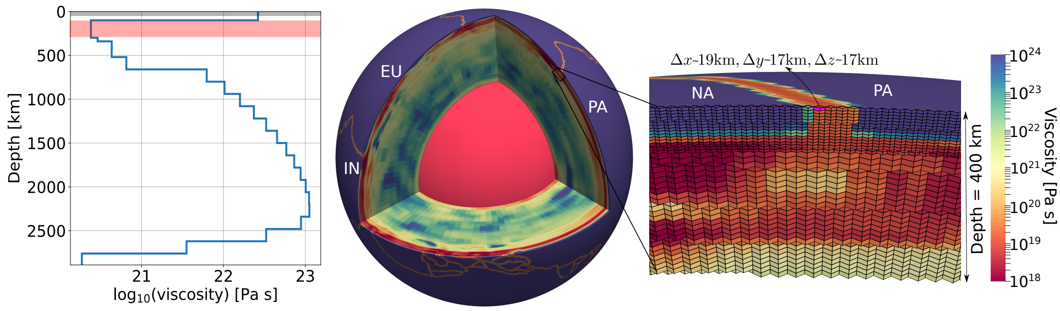

Figure 2. (left) Reference viscosity profile from Steinberger and Calderwood (2006) with a modified low-viscosity asthenosphere extending until 300 km depth (pink layer). (right) Model setup with a cut-out section illustrating the heterogeneous lateral and radial viscosity distribution and a magnified view of the the Aleutian slab showing the mesh geometry adopted in our models. The narrow red zones at the surface represent the imposed plate boundaries where viscosities are several orders of magnitude lower than in the surrounding lithosphere. The abbreviations represent tectonic plates: EU (Eurasian), PA (Pacific), NA (North American) and IN (Indian) plate.

2.4 Density distribution

We base the density in our model on the temperature distribution and seismic velocity anomalies described in the previous section. Above 200 km, we compute the density from the thermal anomalies in the TM1 model relative to a reference temperature of 293 K as done by Osei Tutu, Sobolev, et al. (2018). We use constant thermal expansion coefficients and compressibilities within the crust, lithospheric mantle and asthenosphere (Osei Tutu, Steinberger, et al., 2018), respectively. To define the crust and the lithosphere, we use the lithospheric thickness from Priestley et al. (2018) and crustal thicknesses from the crust1.0 model (Laske et al., 2012).

Below 200 km, we infer the density from seismic tomography. Specifically, we use a depth-dependent scaling factor to convert S-wave velocity anomalies to density (Steinberger & Calderwood, 2006).

2.5 Rheology

The rheology of our model is purely viscous, temperature- and depth-dependent, and uses an Arrhenius law to describe the different creep mechanisms. We use a combined diffusion/dislocation rheology in the upper mantle and transition zone, and we assume that diffusion creep is dominant in the lower mantle. Prefactors, activation energies and volumes for diffusion and dislocation creep for each major mantle phase are listed in Table 1. To use such a nonlinear viscosity, but simultaneously achieve a viscosity profile that is consistent with constraints from mineral physics and surface observations, we additionally scale the viscosity in each layer of our model so that its lateral average matches the preferred profile of Steinberger and Calderwood (2006) as shown in the left panel of Figure 2. In order to generate a rigid lithosphere, we do not scale viscosities above 60 km depth (gray layer in the left panel of Figure 2). Furthermore, we globally limit the viscosity to make solving the resulting linear system easier. The lower bound is 10^{18} Pa s or the prescribed asthenosphere or fault viscosity, whichever value is lower. The upper bound is 10^{24} Pa s. An example of the resulting viscosity variations is shown in Figure 2 (center). Since the viscosity scaling to the reference profile affects the stresses and strain rates in the model, which in turn influence the dislocation creep viscosity, the combined

Table 1. Flow law parameters used for viscosity

Parameter	Olivine	Wadsleyite	Ringwoodite	Lower Mantle
Diffusion activation energy, E_{diff} (J/mol)	370×10^3	231×10^3	270×10^3	299×10^3
Diffusion activation volume, V_{diff} (m^3/mol)	6×10^{-6}	6×10^{-6}	6×10^{-6}	6×10^{-6}
Diffusion creep stress exponent, n_{diff}	1	1	1	1
Diffusion creep grain size exponent, m_{diff}	3	3	3	3
Diffusion creep prefactor, A_{diff} Pa^{-1}s^{-1}	1.25×10^{-15}	6.12×10^{-19}	2.94×10^{-17}	5.4×10^{-22}
Grain size, d (m)	5×10^{-3}	5×10^{-3}	5×10^{-3}	5×10^{-3}
Dislocation activation energy, E_{disc} (J/mol)	530×10^3	530×10^3	530×10^3	530×10^3
Dislocation activation volume, V_{disc} (m^3/mol)	1.4×10^{-5}	1.7×10^{-5}	1.7×10^{-5}	0
Dislocation creep stress exponent, n_{disc}	3.5	3.5	3.5	3.5
Dislocation creep prefactor, A_{disc} Pa^{-1}s^{-1}	8.33×10^{-15}	2.05×10^{-12}	2.05×10^{-19}	1×10^{-40}

rheology is nonlinear, and requires an iterative solution scheme. We use a fixed-point iteration scheme with a nonlinear solver tolerance of 10^{-4} when solving equations (1) and (2).

To facilitate plate-like deformation in our models, we prescribe plate boundaries as narrow weak zones of reduced viscosity (Figure 2, right panel), taking their locations from global plate models and fault databases (see Section 2.6.1). We import these plate boundaries into ASPECT using Worldbuilder (Fraters et al., 2019; Fraters, 2021), an open source software that facilitates the setup of complex geometries in geodynamic models. We test 4 different input plate boundary models to investigate the effect of the exact plate geometry on plate velocities and deformation patterns. Within the weak zones we fix the viscosity to a constant value that is 3 to 6 orders of magnitude lower than in the surrounding lithosphere (see Table 2 and Section 3.1). This weakening is applied over a width of 50 km, with the prescribed fault traces at the center. Around this weak zone, the viscosity transitions to the value of the surrounding lithosphere following a hyperbolic tangent along each side of the fault.

We note that in reality, brittle failure would create essentially discrete faults in the crust, and even lithospheric shear zones are generally much thinner than the weak zones in our models. Our premise here is that a weak zone of a finite width with an appropriately chosen viscosity can approximate the behavior of more complex rheologies sufficiently well to allow accurate plate motion models on continental and global scales. Our approach contains a trade-off between the thickness and the viscosity of a weak zone. For a given driving force, the same relative velocities between plates can be obtained in a model with a thinner and lower-viscosity weak zone on the one hand, or a thicker less-weak zone one the other hand. We have chosen a shear zone thickness that is appropriately resolved by several mesh cells in our standard resolution, which at the same time ensures we adequately resolve deformation around and inside the weak zone, and makes solving the equations computationally simpler. However, this means that the optimal viscosity in the weak zones in our models is not indicative of the actual viscosity in plate boundary zones on Earth, which display much more complex deformation processes.

2.6 Set of model configurations

In order to constrain the importance of the different model components and the associated plate driving and resisting forces, we vary the following model parameters:

1. the geometry of the plates and plate boundaries,
2. the prescribed viscosity of the plate boundaries (controls friction between plates),
3. the reference viscosity of the asthenosphere (controls the friction at the base of the plate),
4. the strength of cratons (also controls the friction at the base of the plate),
5. the temperature distribution in the model (controls slab pull forces), and
6. the viscosity of subducted slabs (controls how well negative buoyancy forces from slabs are transferred to the plates).

We describe each of these parameters in detail below. A summary of the varied parameters is given in Table 2.

2.6.1 Plate boundary geometry

The general location and distribution of global plate boundaries is relatively well known. However, their individual structure and precise location varies between different plate boundary models. Additionally, depending on the source data used to determine plate boundary locations, they may be closed or open, and they may include only clearly defined plate boundaries, or additional diffuse fault zones. We take this uncertainty into account by using a number of different fault database models to determine the locations of weak zones in our models. Previous work has demonstrated that the geometry and location of weak zones significantly influences the deformation patterns within a model (Van Wijk, 2005; Balázs et al., 2018), however to our knowledge, such an analysis has not been done in global mantle flow models. Therefore, it is unclear how a small change in the geometry of plate boundaries will exactly influence global plate motions, and what type of plate boundary model will reproduce present-day observations best. We use four different fault database models to evaluate their effects on the surface plate motions: Nuvel (DeMets et al., 1990), Bird closed plate boundaries (Bird, 2003) (Bird-closed), the Global Earthquake Model (Pagani et al., 2018; Styron & Pagani, 2020) (GEM), and a limited subset of GEM (Bird-GEM) (Fig 3). The Bird-GEM model is derived from GEM, but uses only the faults at Bird (2003)'s plate boundaries without any intraplate faults or diffused deformation zones. Specifically, the model includes oceanic boundaries similar to the plate boundaries defined in the Bird closed plate boundaries model, but does not include plate boundaries within continental regions (Bird, 2003). Since GEM represents the locations of high seismic hazard (Pagani et al., 2018) and not rigid plates with respective Euler poles—as is generally done to describe tectonic plates (DeMets et al., 1990; Bird, 2003)—the faults in the GEM and Bird-GEM models do not necessarily map into closed polygons (Figure 3), while the boundaries in the Nuvel and Bird-closed models do. Another difference between the fault models is that both GEM and Bird-GEM models have dipping faults based on the seismicity distribution used to develop the GEM model, while we impose vertical plate boundaries in the Nuvel and Bird-closed models. The plate boundary shear zones in all models extend until the lithospheric depth defined by Priestley et al. (2018), except in the case of intraplate deformation in the GEM model where we use the fault depths included in the database.

2.6.2 Friction between plates and at the base of plates

Global surface velocities are influenced by the plate boundary friction and the friction at the base of the lithosphere as observed in previous mantle convection models (Alisic et al., 2012; Osei Tutu, Sobolev, et al., 2018). In particular, the importance of friction at cratonic roots is illustrated by the fact that plate speed decreases with increasing continent area (Forsyth & Uyeda, 1975).

We set the viscosity within the plate boundaries to a constant value that is three to six orders of magnitude lower than the value of 10^{24} Pa s in the surrounding litho-

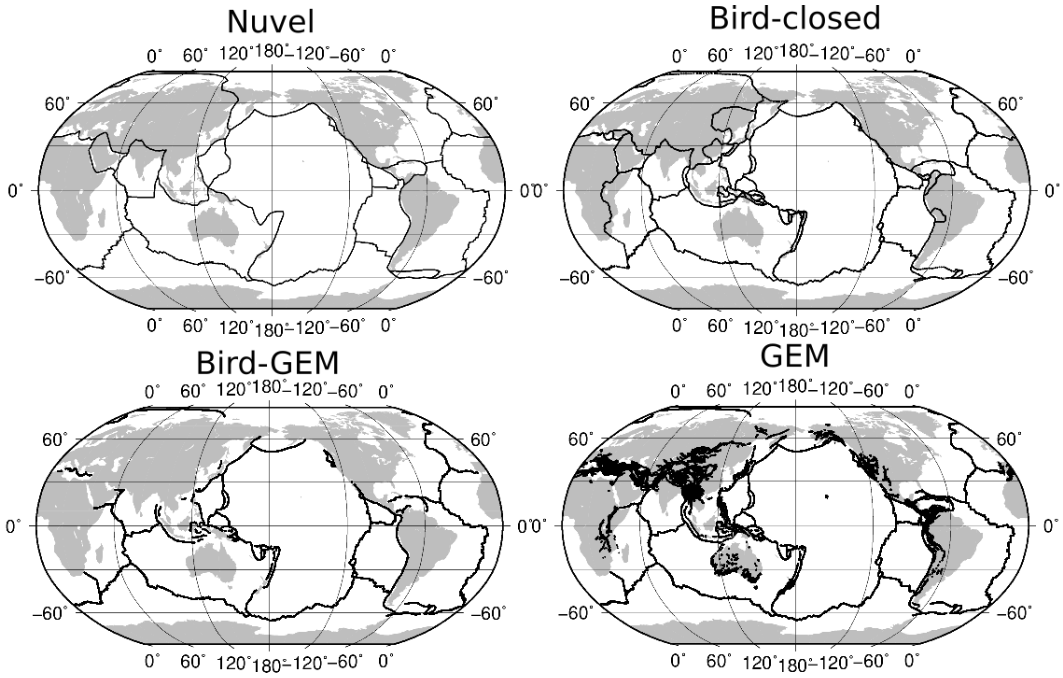

Figure 3. Plate boundary models used in our model setup. See text for details about these models.

Table 2. Parameter values investigated in this study (reference model in bold).

Plate boundary viscosity (Pa·s)	Asthenosphere viscosity (Pa·s)	Plate boundary model*
10^{21}	5×10^{19}	Nuvel
5×10^{20} •	10^{19}	Bird-closed
$\mathbf{2.5 \times 10^{20}}$ •	5×10^{18} •	**GEM**
10^{20} •	10^{18} •	Bird-GEM
5×10^{19} •	$\mathbf{5 \times 10^{17}}$ •	
10^{19}		
10^{18}		

*See text for the references to the plate boundary models. Values marked with a • represent runs we selected for all plate boundary configurations after the initial parameter analysis.

sphere to allow for plate-like surface motions (Table 2, see also Section 2.5). In addition, we vary the viscosity of the asthenosphere layer—in our case defined as the sublithospheric mantle down to 300 km depth, see pink layer in the left panel of Figure 2—in our reference viscosity profile taken from Steinberger and Calderwood (2006). Specifically, we reduce the asthenosphere viscosity from the reference value of $2.4{\times}10^{20}$ Pa s to a range of values between 5×10^{19} Pa s and 5×10^{17} Pa s (Table 2). Since basal drag is a resisting force in most cases, a low-viscosity asthenosphere implies lower frictional resistance to the motion of the overlying plates and is expected to lead to faster plate speeds.

2.6.3 Slab and craton strength

After determining the most realistic values for asthenospheric viscosity, plate boundary model, and plate boundary viscosity by analyzing the fit to the direction and the speed of plate motions, we also investigate the influence of the strength of cratons and slabs in this best-fit model. The strength of slabs controls the stress partitioning in the lithosphere and thus affects surface plate motions (Billen & Hirth, 2007; Alisic et al., 2010). Therefore, global mantle flow models often introduce highly viscous slabs to better match observed surface velocities (Wu et al., 2008; Alisic et al., 2010). Because we scale the average viscosity in each depth layer of our model to match a reference viscosity profile (Steinberger & Calderwood, 2006), the scaled viscosity of our slabs in the weak asthenosphere is lower compared to the viscosity value that would result purely from the use of our Arrhenius law at low temperatures. To test the impact of stronger slabs, we remove this scaling of the viscosity in the parts of the asthenosphere where non-adiabatic temperatures are below -100 K. This ensures that the slab viscosity is not decreased through re-scaling as the rest of the asthenosphere, allowing us to quantify the effect of the strength of slabs on the plate motions. We note that this algorithm also increases the viscosity in the colder regions below the cratonic lithosphere, since the scaling is not applied to those areas either.

The strength of cratons impacts the plate–mantle coupling, which can affect plate velocities (Conrad & Lithgow-Bertelloni, 2006; Rolf & Tackley, 2011; Osei Tutu, Sobolev, et al., 2018). Therefore, we investigate the influence of strong cratons in our models, using locations from Nataf and Ricard (1996). In regions defined as cratons, we increase the viscosity within the lithosphere to 10^{25} Pa s, compared to the surrounding lithospheric viscosity of 10^{24} Pa s. Within the cratons, we also set the lithosphere density to our reference adiabatic profile. This makes cratons neutrally buoyant and compensates for compositional density differences within the cratonic lithosphere.

2.6.4 Temperature distribution

In order to quantify the influence of the different sources of buoyancy in our models, we varied the temperature distribution of the model configuration that yielded the best fit to the observed plate motions in the above-mentioned parameter study (asthenosphere viscosity of $5{\times}10^{17}$ Pa s, GEM plate boundary model (Pagani et al., 2018), and plate boundary viscosity of $2.5{\times}10^{20}$ Pa s). To quantify the influence of buoyancy forces, specifically slab pull associated with the temperature distribution based on seismic tomography, we ran a model that only includes the temperature variations from TM1 and has an "empty" mantle below 200 km depth. Second, to investigate the effect of slab pull in the upper mantle, we ran a model that only included an adiabatic temperature profile in the sub-lithospheric mantle in the upppermost 200 km—in other words, the only temperature heterogeneities come from lithospheric thickness variations—and the LLNL-G3D-JPS tomography model below. Third, we want to account for uncertainties in lithospheric thickness and further investigate the importance of viscous drag within the uppermost mantle (i.e., 200 km) compared to the underlying convective flow. For this purpose, we run models where we shift the temperatures from the TM1 model in the uppermost mantle by 30 km (both upwards and downwards) to represent a thinner and a thicker lithosphere, respectively (see Supporting Information).

2.7 Misfit analysis

To quantify how well our models reproduce the observed plate motions, we compare the modeled surface velocities ($\mathbf{u}^{\text{model}}$) to observed GPS velocities ($\mathbf{u}^{\text{obs}}$) in a no-net rotation frame (Kreemer & Holt, 2001). We compute three different indicators:

1. The root-mean-square boundary velocity residual, i.e. $\delta V_{\text{rms}} = \left(\frac{1}{S}\int_S \|\mathbf{u}^{\text{obs}} - \mathbf{u}^{\text{model}}\|^2 dS\right)^{\frac{1}{2}}$, where $\|\cdot\|$ denotes the L_2-norm and S the surface area of the model. The RMS velocity residual provides the most objective measure for the difference between model and plate velocities. While it cannot distinguish *how* the velocities in the model differ from observations, it is the best measure to assess the fit between the models and reality.
2. The angular correlation-like measure $\xi = \dfrac{\int_S \|\mathbf{u}^{\text{obs}}\|^2\, \hat{\mathbf{u}}^{\text{obs}} \cdot \hat{\mathbf{u}}^{\text{model}}\, dS}{\int_S \|\mathbf{u}^{\text{obs}}\|^2 dS}$, where $\hat{\mathbf{u}}$ represents the respective normalized unit vectors. ξ allows us to identify how much of the misfit is caused by the direction of plate motion. This angular mean is weighted by the square of the observed velocity magnitudes to give more weight to regions that exhibit stronger flow. This measure is similar to the angular correlation defined by Becker (2006); Liu and King (2022), except that they use the product of observed and modeled velocity magnitudes as weights whereas we use only the observed velocities to avoid giving not enough weight to areas where the modeled velocities are very small. ξ varies between -1 and 1, where a value of 1 corresponds to a perfect correlation between observed and modeled plate motion directions. Our modification of the definition results in overall lower values of ξ for all models. To be able to compare our results to Becker (2006); Liu and King (2022), we provide both measures in Section 3.5.3.
3. The mean speed residual, i.e., $\frac{1}{S}\int_S \|\mathbf{u}^{\text{obs}}\| - \|\mathbf{u}^{\text{model}}\| dS$. The mean speed residual allows us to identify how much of the misfit is caused by the speed of plate motion. The misfit in absence of any plate motion would be 3.8 cm/yr, which is the mean speed of the GPS data. Note that this misfit is computed as integral of the point-wise difference between the velocity magnitudes. It is not the difference in the average speed of all plate motion, as done in some other studies.

We have implemented the computation of the root-mean-square boundary velocity residual as a postprocessor in ASPECT so that it is available to the community for future studies. In addition, we provide scripts to compute the angular correlation and speed residual as data publication (Saxena et al., 2022).

3 Results

3.1 Influence of plate boundary weakness and basal drag

To obtain a good fit between our dynamic models and the observed plate motions, we varied the influence of the asthenospheric viscosity (affecting the amount of basal drag on the plates) and the plate boundary viscosity (affecting friction between plates). For this parameter study, we used the Bird closed plate boundary geometry. Our results (Figure 4) show that both parameters have a strong influence on the speed and the direction of plate motion. The speed of plates increases both for lower asthenosphere viscosities and weaker plate boundaries as indicated by the increased velocity residuals for these values. However, the plate boundary viscosity affects the plate motions considerably more: The RMS velocity and mean speed residuals (Figure S1) are reduced by an order of magnitude as the plate boundary viscosity increases from 10^{18} Pa s to 10^{20} Pa s. A further increase in plate boundary viscosity to 10^{21} Pa s slightly increases these residuals again for all chosen values of asthenospheric viscosity. On the other hand, the fit to the direction of plate motion generally improves with increasing fault viscosity, and we achieve the best directional fits of $\xi = 0.87...0.91$ for fault viscosities of 10^{21} Pa s (see Table S2). This value is consistent with the results of both Liu and King (2022), whose best-fitting viscosity model also has a plate boundary viscosity of 10^{21} Pa s, and Ghosh and Holt (2012), who used a spatially variable viscosity in their plate boundary zones based on strain rate magnitudes in a global kinematic model and achieved a good fit for vis-

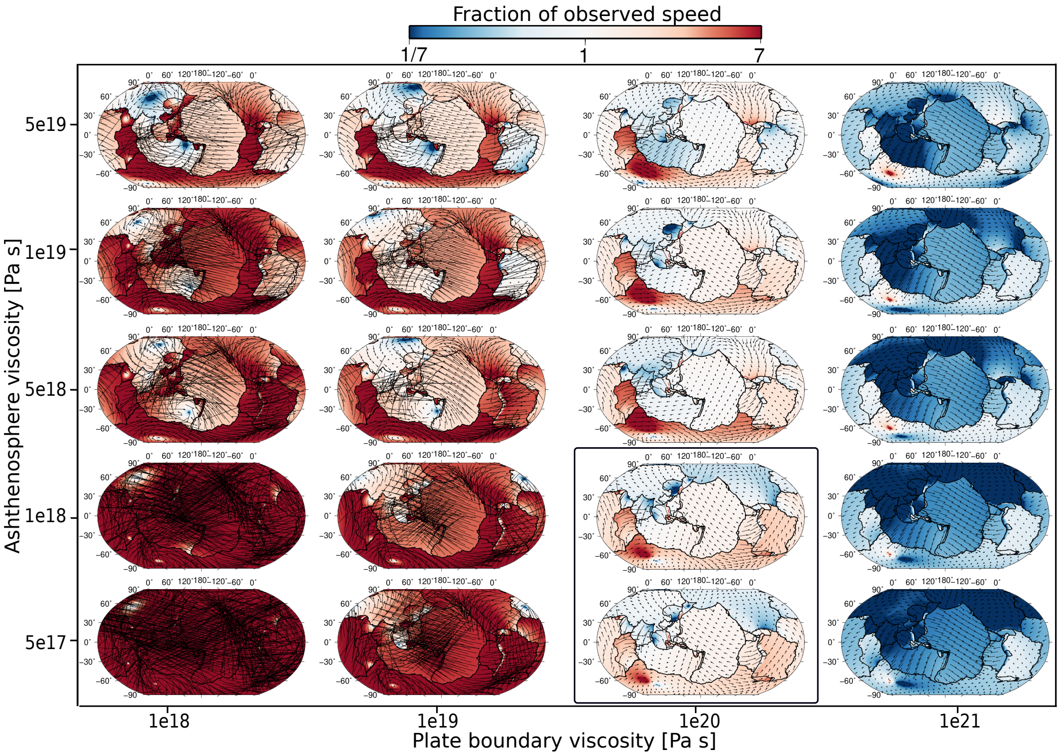

Figure 4. Fraction of modeled speed relative to the observed GPS speeds at the surface for different combinations of plate boundary viscosity and asthenosphere viscosity, and using the Bird-closed plate boundary model (Bird, 2003). The arrows represent point-wise differences between modeled and observed velocity vectors. The black box marks the models with the lowest RMS velocity residual.

cosities varying between 10^{20} and 10^{22} Pa s. However, this general trend is very different from the results of Osei Tutu, Sobolev, et al. (2018), who include plastic yielding at plate boundaries and find that increasing the plate boundary friction coefficient also increases the angular misfit, especially for low asthenosphere viscosities. Our models with the overall best (RMS velocity) fit have intermediate plate boundary viscosities ($\approx 10^{20}$ Pa s) and low to intermediate asthenosphere viscosities ($\leq 10^{18}$ Pa s).

If the plate boundary viscosity is higher than $\approx 10^{20}$ Pa s, all plates are moving too slowly (Figure 4, right column). Since the high plate boundary strength controls plate motions, the speed remains almost unchanged for different asthenosphere viscosities.

Conversely, if the asthenosphere viscosity is high, but the fault viscosity is low, basal drag controls the plate motion. In this case, the smallest plates move too fast, especially the ones directly attached to subducted slabs (Nazca, Arabian, Cocos, Philippine plates), but also many of the very small plates of the Bird model that are not considered in the Nuvel model, like Scotia and the smaller plates near Indonesia (Figure 4, top left panels). This can be explained by smaller plates having a higher ratio of plate boundary length over area. In other words: Smaller plates are controlled more by the friction at their boundaries, whereas larger plates are influenced more by the friction at their base. Consequently, weak plate boundaries allow the small plates to move much faster than they should, whereas large plates are still limited in their speed. If both viscosities are low, all plates simply move too fast, and the overall residual is large everywhere (Figure 4, bottom left panels).

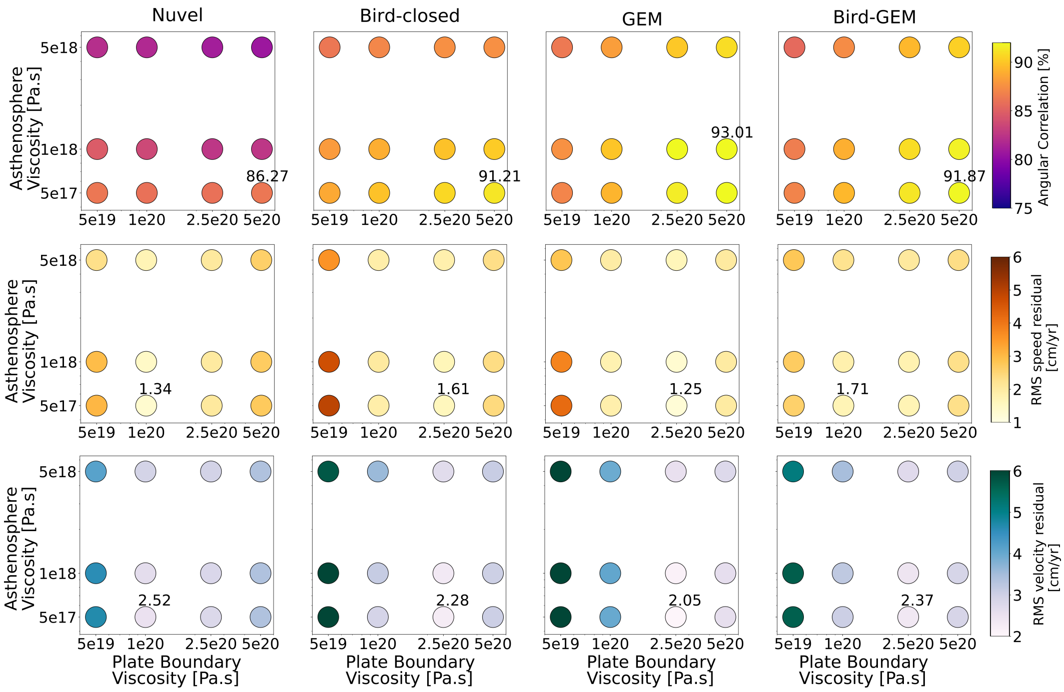

Figure 5. Angular correlation, mean speed residuals and velocity residuals between modeled and observed GPS velocities at the surface for different values of fault viscosities and asthenosphere viscosities for different plate boundary models (as in Figure 3). Maximum angular correlation, minimum speed residual, and minimum RMS velocity residual are annotated in each subplot. Note that in all plots light colors represent a good fit, and saturated colors represent significant misfits.

3.2 Influence of plate boundary geometry

In a second step, we picked a subset of parameter values close to the model that achieved the best fit to observed plate motions (Figure 4), specifically, plate boundary viscosities of 5×10^{19} to 5×10^{20} Pa s, and asthenosphere viscosities between 5×10^{17} and $5{\times}10^{18}$ Pa s, and tested the influence of different plate boundary geometries (see Section 2.6.1). The resulting angular correlation, speed and RMS velocity residuals are shown in Figure 5. The choice of plate boundary model strongly influences the resulting plate motions (see also Figure 6) and therefore, the computed misfit (see Figures S2–S5 for maps of the velocity residuals). While the general trends we describe in Section 3.1 remain unchanged, we find an improved fit to the speed and a slightly better fit to the direction of plate motion. Specifically, the models based on the GEM database (GEM and Bird-GEM in Figure 3), which do not have closed plate boundaries, and which include information about the dip of plate boundaries, produce better weighted angular correlations for all models, reaching values around $\xi = 0.92$. The GEM plate boundaries also achieve the best overall fits indicated by the RMS velocity residual. Specifically, the best fitting model (with an RMS velocity residual of 2.05 cm/yr) has an asthenosphere viscosity of $5{\times}10^{18}$ Pa s and a plate boundary viscosity of $2.5{\times}10^{20}$ Pa s. However, all GEM models with plate boundary viscosities of $2.5{\times}10^{20}$ Pa s reach good overall fits with RMS velocity residuals below 2.5 cm/yr.

These results show that the plate boundary geometry plays a crucial role for the direction of plate motions and that the presence of closed plate polygons in geodynamic models as implemented in previous mantle convection models (e.g., Stadler et al., 2010; Osei Tutu, Sobolev, et al., 2018; Liu & King, 2022) is not essential. It seems to be a better approximation of the plate boundary rheology to have clearly defined weak plate boundaries only in some regions (for example, at subduction zones and mid-ocean ridges), and more distributed deformation, where stress can be transferred between plates, in other places. Specifically, many regions where the plate boundaries are not closed in the Bird-GEM model and where the GEM model features regions with a diffuse fault network indicate what Bird (2003) labels as “orogens”, areas where deformation is complex and it is very difficult to define plates, because there is so much seismic, geologic, and geodetic evidence for distributed anelastic deformation. In the models based on the GEM database, weak zones in these complex regions only extend to crustal (seismogenic) depths, which achieves a better fit than the models with closed plate polygons. The Bird-closed and the Bird-GEM models do not perform as well as the GEM models, but better than Nuvel, and the residuals for their respective best-fit models are similar. This suggests that even without the diffuse fault network of the GEM database, discrete weak boundaries in the continental regions—as in the Bird-closed models—do not improve the modeled velocities considerably compared to a model that features strong continental regions with more distributed deformation, such as Bird-GEM. The Nuvel model, which is most commonly used for geodynamic models, performs substantially worse than the other plate boundary models, in particular in terms of angular fit. It can either fit the fast-moving oceanic plates, but then the slow motion of the South American and Antarctic plates is not reproduced well (see Figure S2, models with plate boundary viscosity of 10^{20} Pa s and asthenosphere viscosity of 10^{18} Pa s or below), or it fits the slower continental plates, but velocities are not high enough for the Pacific and Australian plates (models with plate boundary viscosity of $2.5{\times}10^{20}$ Pa s or higher). The GEM, Bird-GEM, and Bird-closed models provide a reasonably good fit to all of these plates in the best-performing model (Figure 6), with in particular the Eurasian, North American and South American plate showing lower RMS residuals in the GEM model. On the other hand, many of the smaller plates in the Western Pacific that consistently show large RMS velocity errors in the Bird plate boundary models (Caroline, North Bismarck, South Bismarck) show an improved fit when using the Nuvel plate geometry, indicating that their rheology is better approximated by one large plate rather than several smaller ones.

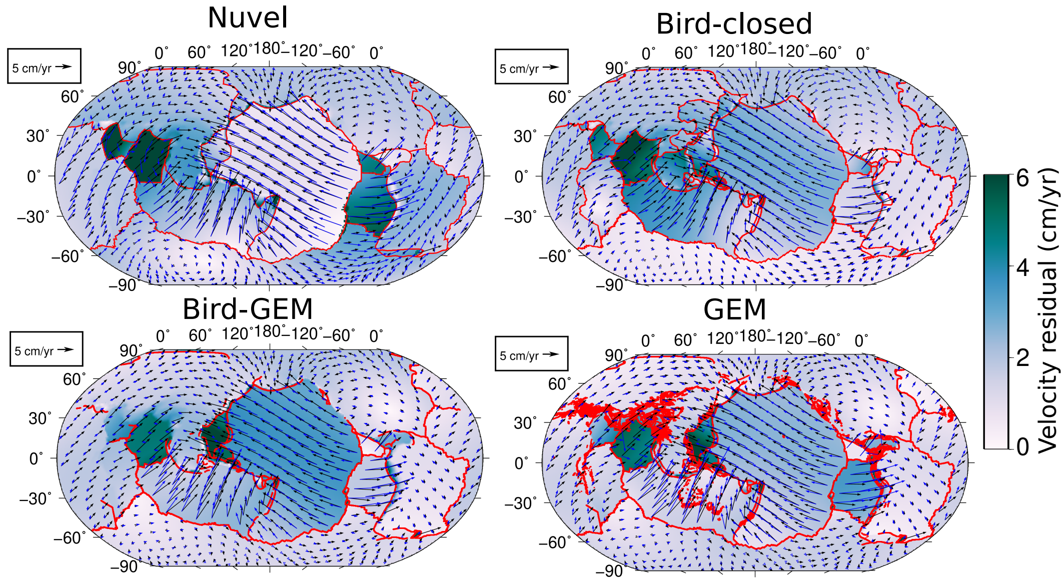

Figure 6. Velocity residual (background colors), together with the modeled velocity at the surface (blue arrows) and the observed GPS velocities (black arrows; Kreemer & Holt, 2001) for the different plate boundary models marked in red. For each plate boundary model, we show the model with the fault and asthenosphere viscosity values that achieve the lowest RMS velocity residual in our parameter study (Figure 5).

Our results indicate that different types of plate boundaries have different rheologies, and using a plate boundary model with closed polygons where all plate boundaries have the same strength is not a good approximation of plate tectonics on Earth. In particular, assuming that subduction zones and mid-ocean ridges are substantially weaker than orogenic zones and continental rifts yields a better fit to global plate motions. This result is consistent with Osei Tutu, Sobolev, et al. (2018)'s analysis, who find an improved directional fit of most plates when using weaker subducting plate boundaries compared to the other plate boundaries.

3.3 Reference model

The model that fits the observed plate motions best uses the GEM plate geometry and has an asthenosphere viscosity of 5×10^{17} Pa s and a plate boundary viscosity of $2.5{\times}10^{20}$ Pa s. This model features an RMS velocity residual of 2.05 cm/yr, an angular correlation of $\sim$91% (94.5% in the measure of Becker, 2006; Liu & King, 2022) and a speed residual of 1.25 cm/yr. These values are comparable to previous studies (see below). The RMS velocity indicates that plates in our model are slightly slower than observed plate velocities, and the angular correlation shows a good fit to present-day plate directions. Comparing individual plates (Figure 6, bottom right) shows that the motion of the African, North American, South American and Eurasian plates are in good agreement with the observations, while most of the residual is concentrated in the smaller plates (Nazca, Indian, Philippines). The oceanic plates, and in particular the Pacific, Nazca and Cocos plate, have a very high correlation of the direction of plate motion (Figure 7, left). This is expected, since they are pulled in the direction of the slabs that are attached to them. On the other hand, they also have a low to moderate speed residual (Figure 7, right), with the Pacific plate moving slightly too slowly and the smaller Nazca plate moving too fast. This could indicate that our chosen plate boundary viscosity is slightly too low compared to the asthenosphere viscosity, since smaller plates have a higher ratio of

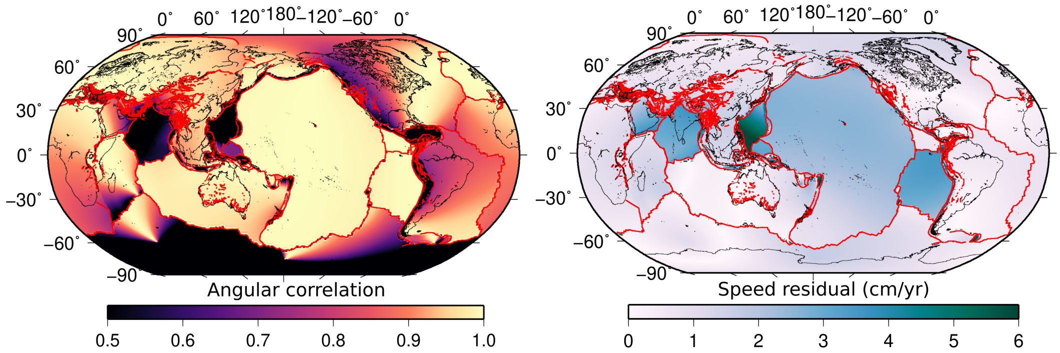

Figure 7. Map of angular correlation and speed residual for our reference model.

plate boundary length over area so that weak plate boundaries allow them to move quickly, especially if they are pulled by a slab (see Section 3.1). The Cocos plate is an exception, showing a good match with the observed GPS velocities both in direction and speeds. The Philippine plate does not fit this pattern either, having a poor fit both in terms of direction and speed of plate motion. This could be caused by a misalignment between the slab locations in our temperature model (which are vertically downward, based on the TM1 model) and the dipping weak zones in our plate model (which are dipping as recorded in the GEM database). Being attached to the Izu-Bonin/Mariana slab instead of or in addition to the Ryukyu and Manila slabs might cause the Philippine plate in our model to move much more slowly than observed.

In contrast to the oceanic plates, the continental plates exhibit a lower angular correlation, in particular the South American plate, the Indian plate, and the Antarctic plate. However, they have a small speed residual, in part also owing to their lower overall speed, causing them to contribute less to the global misfit of the plate motions.

Previous studies have achieved angular correlations in the range of 86–96%, similar to our value of $\sim$91.5%. Specifically, the angular correlation is between approximately 86 and 88% in Conrad and Lithgow-Bertelloni (2002, Figure S1), $\xi = 0.95$ in the best-fit model of Becker (2006) that uses a laboratory-derived viscosity law, the angular misfit is around 10% and 8% in Alisic et al. (2012, Figure 4) and Osei Tutu, Sobolev, et al. (2018), respectively, and $\xi = 0.957$ in Liu and King (2022). We note that both Becker (2006) and Liu and King (2022) weigh their angular fits with the product of modeled and GPS velocities instead of using only the observed velocities as we do here. Using their measure of fit, our best-fit model has an angular fit of 94.5%. The speed of plate motions is more difficult to compare, since different studies use different measures. In Conrad and Lithgow-Bertelloni (2002), the plate speed is a tuning parameter of the model, since it is normalized to the average plate speed by adapting the asthenosphere viscosity. Becker (2006) and Liu and King (2022) use the mean logarithmic amplitude ratio β to compare modeled and observed plate speed, and achieve $\beta \approx -0.22$ and $\beta = -0.047$, respectively. In this measure, $\beta = 0$ would indicate a perfect fit to the observed plate speed; and our best-fit model achieves a comparable fit of $\beta = -0.13$. We note that since β is calculated as $\sum_{i=1}^{n} \log_{10}(\mathbf{u_i^{model}}/\mathbf{u_i^{obs}})$, it is possible to have a small β value if some plates are faster and others slower than the observed speed, as long as they compensate each other in the mean, while our measure of the speed residual uses the absolute value of the difference between modeled and observed speeds before integrating over the surface (see Section 2.7). Osei Tutu, Sobolev, et al. (2018) report a root mean square velocity error of 38% (their fig 6, dark blue line), corresponding to a speed residual of 1.44 cm/yr, slightly larger than our value of 1.25 cm/yr. Ghosh and Holt (2012) achieve an RMS misfit of $\sim$1 cm/year, which is somewhat lower than our RMS residual of 2 cm/yr, however, note that Ghosh and Holt (2012) assimilate observed deformation into their model setup by using a variable plate boundary viscosity proportional to the inverse of the observed strain rate. Both Stadler et al. (2010) and Alisic et al. (2012) use different measures of evaluating their model fit, preventing us from performing a quantitative comparison.

While the overall fit is similar to previous studies, one noteworthy point is that our models reproduce the motions of the North American plate well, something that has been difficult to achieve in previous modeling studies (Liu & King, 2022). Here, the key feature that improves this fit is the use of the open (Bird-GEM or GEM) rather than closed plate boundaries along the western North American continent (Figure 6).

3.3.1 Modeled strain rates

To assess how well our best-fit model matches observed deformation rates, we compute the second invariant of the strain rate ($\dot{\varepsilon}_{II}$) and compare it with the recent Global Strain Rate Model (GSRM; Kreemer et al., 2014) in Figure 8. Both modeled and observed $\dot{\varepsilon}_{II}$ have characteristic types of deformation that can be classified into three distinct categories: (1) slowly-deforming intraplate regions, (2) plate boundaries, and (3) regions of distributed deformation. The slowly-deforming intraplate regions feature low strain rates, in our model they are of the order $\sim 10^{-17}$ s^{-1}, in GSRM these are assumed to be rigid and not allowed to deform, i.e., the strain rate is not defined in these regions. Our modeled values are similar to the expected strain rates within a rigid lithosphere (Gordon, 1998; Zoback et al., 2002), and are consistent with geodetic studies of stable intraplate regions (Calais & Stein, 2009; Braun et al., 2009) and previous global mantle convection models (Ghosh & Holt, 2012). The narrow zones of high deformation along the prescribed plate boundaries separating the rigid plates feature high strain rates, between 10^{-14} s^{-1} to 10^{-13} s^{-1} in our model and $\gtrsim 10^{-14}$ s^{-1} in GSRM. Lithosphere with more distributed deformation has strain rates of the order of $\sim 10^{-16}$ s^{-1}. In our model, these zones are near the subducting plate boundaries between Nazca–South America, Pacific–Philippine, Cocos–North America, and Pacific–Australia, the continental–continental collision boundary between India-Eurasia, the transform boundaries between Pacific–North America, Scotia–South America, and the divergent boundaries between Somalia–Nubia, and Pacific–Antarctica. With the exception of Pacific–Antarctica, these zones were also defined as regions of broad deformation, which are not part of a rotating rigid plate, in GSRM (Figure 1 in Kreemer et al., 2014). Several of these diffused deformation regions, i.e., along the Nazca–Pacific, India–Eurasia, Pacific–North America, and Pacific–Antarctica plates, are also labeled as "orogens" by Bird (2003). We do not attempt a more quantitative comparison here since the width of our plate boundaries is limited by the achieved model resolution and does not necessarily correspond to the width of plate boundaries on Earth. But it is interesting to note that prescribing these diffuse weak zones only within the crust is enough to concentrate stresses from the lithosphere and deeper mantle at similar locations as observed on Earth (Figure 8)—a result of the heterogeneous viscosity distribution including lateral variations in temperature and lithospheric thickness.

3.3.2 Model resolution

To test how our numerical resolution impacts the results, we rerun our reference model with 4 global and 4 adaptive refinement levels instead of 5 + 2 refinements as used for all other models in this study. This increases the resolution in the uppermost mantle and at the plate boundaries to 8.5 km, while maintaining a lower mantle resolution comparable with the input tomography model. Overall, the results of the higher-resolution model are very similar to our reference model: an angular correlation of 90.5% (reference model: 91%), a mean speed residual of 1.38 cm/yr (reference: 1.25 cm/yr), and a RMS velocity residual of 2.15 cm/yr (reference: 2.05 cm/yr). While we do not observe significant differences in the computed misfits between our standard and the high-resolution

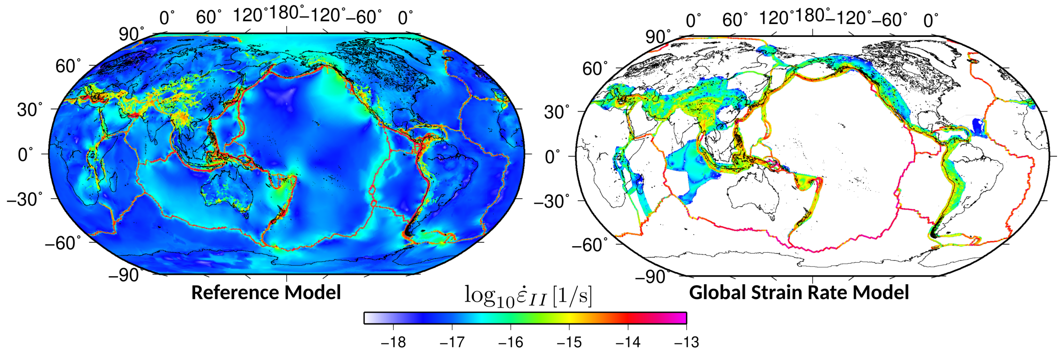

Figure 8. Modeled second invariant of strain rate at the surface for our reference model (left) and from the GSRMv2.1 model (Kreemer et al., 2014).

model, the plates tend to move slightly slower in the high-resolution model. The fact that differences between model resolutions are very small shows that our results are robust with respect to the numerical resolution of the models. We note that in order to keep the results comparable, the width of plate boundaries in the high-resolution model is still the same as in our base model, and larger than the width of lithospheric shear zones on Earth. Reducing this width may affect the model results, and could provide additional insights into plate boundary stresses and rheology in future studies.

3.4 Varying slab and craton strength

As outlined in the previous section, the model configuration with the GEM plate boundaries, an asthenosphere viscosity of 5×10^{17} Pa s, and a plate boundary viscosity of 2.5×10^{20} Pa s achieves the lowest RMS velocity misfit. We therefore use this model as a reference case to test the influence of additional parameters.

For this purpose, we include neutrally buoyant and stiff cratons as described in Section 2.6.3 in our reference model. We then compare the resulting plate motion fit with the original (reference) model (Figure S7). Our results show that the modeled plate velocities in the presence of cratons are only marginally slower than the reference model. Slow-down occurs in particular for the plates that contain cratons. On the other hand, the direction of plate motion is similar to our reference model (see also Table 3). These results suggest that the lithospheric viscosity derived from the colder regions of cratons in our reference model is already strong enough to resist almost all deformation within the continental lithosphere and further increasing the viscosity in the cratonic lithosphere does not affect the plate-mantle coupling. Since lithospheric thickness is the same in the models with and without cratons, this also indicates that the observed anti-correlation between plate speed and continental area (Forsyth & Uyeda, 1975) is predominantly related to the thinner asthenosphere associated with thick cratonic roots rather than increased friction between the asthenosphere and the base of the plate. Our results are consistent with Ghosh et al. (2013), who find a similar global fit to the observed plate motions for models with strong cratons and models with temperature-dependent viscosity, and with the study of Conrad and Lithgow-Bertelloni (2006), who find that the basal tractions on a lithosphere with lateral viscosity variations are similar to those of a lithosphere with only a layered viscosity structure. We do not investigate the effects of varying craton thickness on the plate motions, which will likely change the plate-mantle coupling as observed in previous studies (Zhong, 2001; Conrad & Lithgow-Bertelloni, 2006; Rolf & Tackley, 2011). However, we study the influence of the overall lithospheric thickness (see Supporting Information).

In a separate test, we investigate the influence of stress transfer within slabs in the asthenosphere (see Section 2.6.3). In contrast to the reference model, this configuration does not include the cold regions of the asthenosphere (more than 100 K below the adiabat) when scaling viscosities to adhere to the radial viscosity profile on average. Consequently, subducted slabs, but also cold cratonic roots, have a higher viscosity compared to the reference case, potentially allowing for better transmission of stresses within subducted slabs.

The presence of stiffer cratons and well-connected slabs increases the overall speed of the plates and leads to an improved angular correlation and RMS velocity residual compared to the reference model (see Table 3). This suggests that the effect of improved stress transmission in the stronger slabs slightly surpasses the increased viscous drag around the cold regions, and consequently leads to faster motion of plates and better directional fit to the observations. This is illustrated by the modeled velocities at the surface and along a cross-section cutting through the subducted Nazca slab (Figure 9): The higher viscosity in cold asthenospheric regions in this model (compared to the reference model) improves the connectivity of slabs throughout the asthenosphere, leading to higher slab sinking velocities below the asthenosphere and slightly higher plate velocities. The most substantial velocity increase occurs in the Pacific and Cocos plate, whereas other oceanic plates (Australia and Nazca) do not show higher velocities. The directional change is most significant for the South American and Nazca plates, both aligning better with the observed GPS velocities in the presence of stronger slabs.

Previous studies (Billen & Hirth, 2007; Capitanio et al., 2009) have suggested that stiff slabs, or a stiff slab core, with a viscosity of $10^{24} - 10^{25}$ Pa s, are essential to accurately model plate motions. This strong stress guide is required for transmitting slab pull forces effectively (>70%) through the slab to the subducting plate (Capitanio et al., 2009), and for achieving a high "plateness" of surface velocities (Zhong et al., 1998). The high subducting to nonsubducting plate speed ratio observed on Earth can only be recovered if the buoyancy of upper-mantle slabs is transferred to the plates by slab pull forces rather than slab suction (Conrad & Lithgow-Bertelloni, 2004). However, the increase in oceanic plate speed due to stronger slabs in our models is much smaller than the about two-fold increase in slab pull in presence of a stiffer slab core predicted by Capitanio et al. (2009). In our models, slabs are not as well-defined as in time-dependent geodynamic models of subduction evolution, (1) because we use a tomographic model that to some degree diffuses the temperature anomaly of slabs so that they are too wide and not cold enough, and (2) because our model includes a boundary between two different temperature models at 200 km depth, where slabs are not always well-connected. This reduces the potential for stress transfer along the slab, even if colder regions are more viscous. In addition, the more diffused temperature anomalies counteract one of the key mechanisms that Billen and Hirth (2007) identified for keeping the subducting plate and overriding plate decoupled and allowing slabs to easily subduct through the upper mantle: A reduced viscosity around the slab due to the strain-rate dependence of viscosity. In tomography-based models, temperatures are reduced in a broader region around slabs, leading to wider zones of increased viscosity and suppressing strain localization around the slab. This is one of the main weaknesses of tomography-based instantaneous models and highlights the need for incorporating better slab models into this type of simulation.

To better understand this effect of slab connectivity, we vary the transition depth between the TM1 model and the tomography model in the reference model setup (from 200 km to values between 100 and 300 km, see Table 3). Shallower transition depths imply more connected but diffused slabs (see Section 2.3), whereas deeper transitions imply more defined, but vertical slabs in the uppermost mantle that might be disconnected at the boundary between the two temperature models. We find that the model with a transition depth of 150 km achieves a better fit to the observed plate motions than the

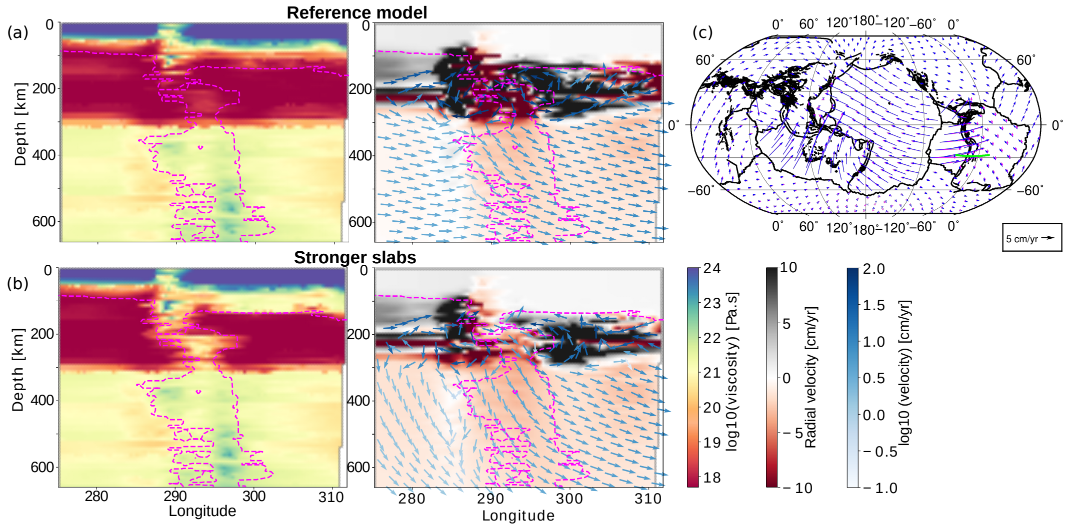

Figure 9. Viscosity distribution and flow field in the upper mantle and transition zone through the Andes subduction zone for the reference model (a) and the model with strong slabs and cratons in the asthenosphere (b). Magenta contours represent the approximate slab and plate location as regions where the non-adiabatic temperature is <-100 K. For clarity, velocity vectors are only plotted below 150 km depth. (c) Modeled velocity at the surface for our reference model (blue) and the model with stiffer slabs and cratons (magenta). The green line marks the location of the cross-section plotted in (a) and (b).

reference model, with a velocity residual of 1.87 cm/yr (compared to 2.05 cm/yr). The main improvement in this model compared to the reference model is the increased speed of the Pacific plate, which is now comparable to the observations. In addition, the Philippine plate now moves in the correct direction, and the angular correlation for South America is improved as well. On the other hand, the speed residuals increase for the Nazca and Cocos plate because they are now moving faster than observed (Figure 10), and the angular correlation of the North American Plate is lower. The higher speed of the oceanic plates is likely due to the better slab connectivity when using a transition depth of 150 km instead of 200 km, as in our reference model. Accordingly, this model is the best-fitting model amongst all the model configurations we tested in this study (see Tables 3 and S2). We note that other plate boundary configurations such as Bird and Bird-GEM achieve the best fit for a transition depth of 200 km instead of 150 km (see Table S1), which is what motivated us to use the value of 200 km for our parameter study presented in Section 3.1.

3.5 Quantifying plate driving forces

In addition, we use our reference model to study how much each of the different components of the model contributes to the observed plate motion. For this purpose, we separately remove buoyancy and viscosity variations from the tomography model (below 200 km depth, TM1_only model), and from the sublithospheric upper mantle above 300 km depth (LLNL_only model).

3.5.1 Influence of upper mantle heterogeneities

Without the driving forces in the transition zone and lower mantle introduced by the tomography model, the plate speed is reduced to about 73% of the reference model,

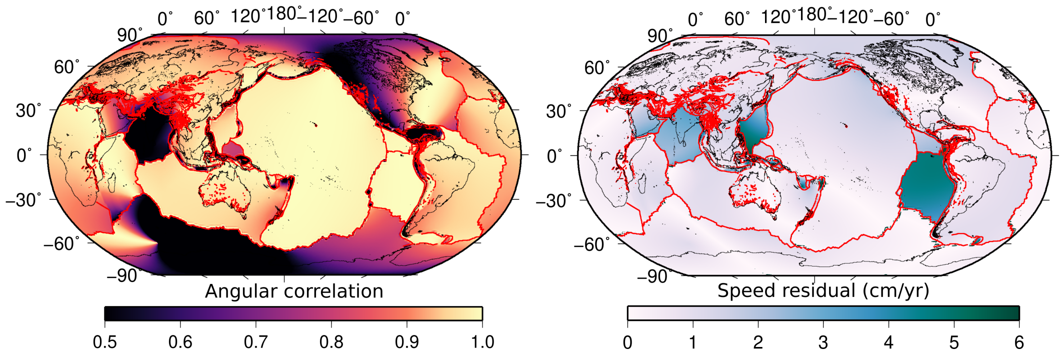

Figure 10. Map of angular correlation and speed residual for our best-fit model.

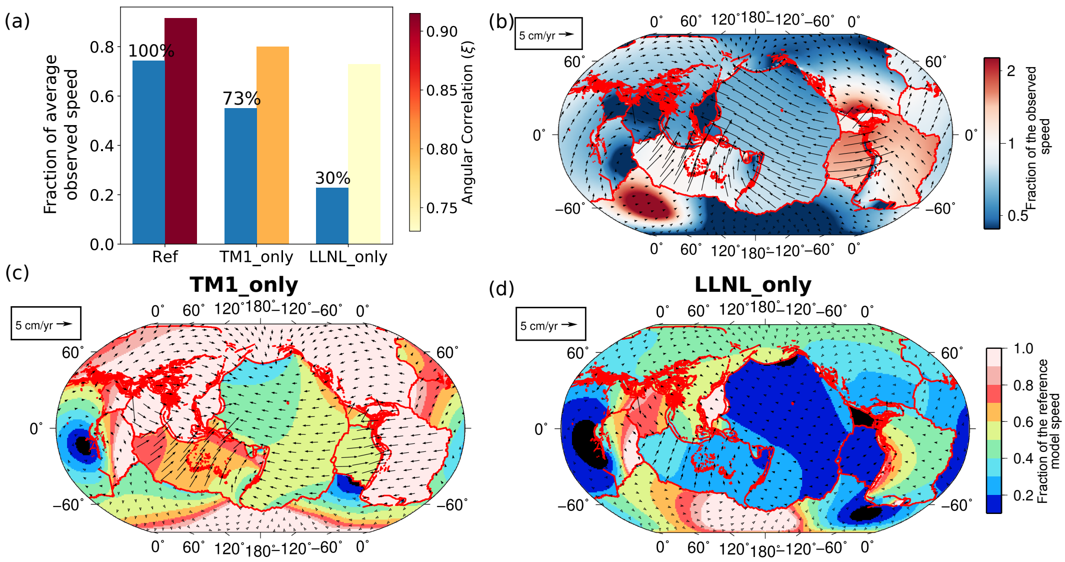

Figure 11. (a) The ratio of averaged modeled speed to averaged observed GPS speed (blue bars) for different models and their respective angular correlation-like measure, ξ. The text on the bars denotes the fraction of average modeled speed relative to average reference model speed. (b) Point-wise fraction of modeled speed in the reference model with respect to the observed GPS speed. (c, d) Point-wise fraction of the modeled speed with respect to our reference model for two models: (c) Model with temperatures based on only the TM1 model above 200 km depth and with a homogeneous mantle below (TM1_only). (d) Model with temperatures based on only the LLNL-G3D-JPS model below 300 km depth and a homogeneous sublithospheric mantle above (LLNL_only).

on average. This means that about three quarters of the observed plate speed can be explained by the forces resulting from heterogeneous mantle structure in the uppermost 200 km of the Earth alone. The velocity reduction associated with removing the mantle structure below 200 km is much stronger in the oceanic plates compared to the continental plates (Figure 11c), indicating that the lower plate speed is caused by a reduction mostly in slab pull forces. While slab pull only acts on subducting plates, slab suction acts equally on all plates (or might have a slightly bigger influence on continental plates due to the higher traction at the plate base). Consequently, a change in slab pull should primarily affect subducting plates, whereas a change in slab suction would affect all plates similarly. But with the exception of the African plate, which is slowed down substantially ($\sim$40% to 50% of the reference model), continental plates speed up or retain most of their speed (Figure 11c). We also attribute this to the low-temperature regions below continental plates generated by cold subducting slabs. These low-temperature regions lead to strong viscous drag at the base of the plate if the heterogeneous mantle structure below 200 km depth is included. If these drag forces are reduced by using a homogeneous mantle below 200 km depth, the plates can move more easily. On the other hand, the African plate, which has no plate subducting beneath it, does slow down. Oceanic plates that have a slab attached to them, except Australia, move only about half as fast in the model with the homogeneous lower mantle, despite still being connected to the slabs prescribed in the TM1 model up until a depth of 200 km. The angular correlation of the predicted plate motions decreases as well from 91.5% to about 80%.

3.5.2 Influence of lower mantle heterogeneities

Without the driving forces from slabs in the asthenosphere, our models retain about 30% of their plate speed. Again, this velocity reduction is stronger in the oceanic plates (which retain 10–30% of their speed) compared to the continental plates (which retain 40–50% of their speed). The angular correlation decreases considerably from 91.5% to 73.6%). Note that the removal of asthenospheric temperature anomalies has a two-fold effect on plate velocities. First, it removes the driving forces from slab buoyancy; second, it removes the higher viscosities that help transfer deeper buoyancy forces to the surface and influence plate motions. Since the density anomalies below 300 km are no longer connected to the plates at the surface, all driving forces in this model result from slab suction/viscous drag and lithospheric structure. Consequently, these forces together explain at least 30% of the speed of plates, with the remaining $\leq$70% being associated with slab pull and the associated stress transfer within slabs.

3.5.3 Comparison to previous studies

The importance of lower mantle versus upper mantle driving forces has been debated in previous studies.

In the study of Osei Tutu, Sobolev, et al. (2018), lower mantle heterogeneities are critical to reproducing plate motions. The angular misfit in their models increases from less than 10% to up to 50% without the density anomalies in the lower mantle, with the largest misfit occurring for the highest friction at plate boundaries. They also estimate that the tractions resulting from buoyancy below 300 km depth provide about 70% of the plate driving force. Conversely, when upper mantle heterogeneities are removed, their models only show a decrease in the root mean square velocity of approximately 20%, retaining about 80% of the plate speed and featuring only a small reduction in the directional fit.

On the other hand, the models of Stadler et al. (2010) fit observed plate motions best without including lower mantle heterogeneities at all. They prescribe subducted slabs as high-viscosity stress guides based on seismicity, and find that extending them into the lower mantle causes overall mantle flow velocities and most oceanic plate velocities to decrease, making convergent velocities at trenches more symmetric. Similarly, the models of Alisic et al. (2012) show that increasing lower mantle temperature variations speeds up overriding plates that are not attached to subducting slabs and slows down subducting plates with slabs that connect to large-wavelength cold anomalies of high viscosity in the lower mantle, such as the Pacific and Australian Plate. However, Alisic et al. (2012) conclude that lower mantle heterogeneities promote an overall increase in plate speeds, in contrast to Stadler et al. (2010).

Conrad and Lithgow-Bertelloni (2002) find that observed plate motions are best predicted if slabs in the upper mantle generate slab pull forces that account for about half of the total driving force on plates. Their models best reproduce present-day plate motions if nearly the entire weight of upper mantle slabs contributes to the slab pull force, but lower mantle slabs contribute to slab suction, being supported by viscous mantle forces. If lower mantle slabs contribute to slab pull as well, the directions and relative speeds of individual plates are poorly reproduced. Similarly, Becker and O'Connell (2001) conclude that both upper and lower mantle driving forces are important, but find a slightly lower contribution of the lower mantle: Out of the total driving forces, they attribute 20–35% to lower mantle buoyancy, 40–60% to upper mantle buoyancy, and 10–30% to lithospheric structure/ridge push (Figure 19 in their study). This means that out of the total mantle contribution of 70–90%, roughly 40% comes from lower mantle heterogeneities. However, in contrast to Conrad and Lithgow-Bertelloni (2002), Becker and O'Connell (2001) find that the angular fit to the observations improves if the viscous drag from upper-mantle slabs acts on both overriding and subducting plates rather than one-sided pull on the subducting plate (their Figure 20).

The differences between studies can be explained by the different rheological properties employed and the associated balance between plate driving forces. The narrow, high-viscosity slabs in Stadler et al. (2010) are prescribed based on seismicity rather than a seismic tomography model, allowing an effective transmission of stresses between the slab tip and the subducting plate. Since we know that the lower mantle is heterogeneous, the deteriorating fit in the models where slabs extend to the lower mantle could indicate that these modeled slabs transmit stresses to a higher degree than the slabs in the Earth's mantle. This reasoning is also consistent with the conclusion of Conrad and Lithgow-Bertelloni (2002) that plate motions are fit best if lower mantle slabs contribute to slab suction but not slab pull. The models of Osei Tutu, Sobolev, et al. (2018) use a Drucker-Prager rheology, which is strongly nonlinear. Consequently, a slight reduction in driving forces can cause a large change in viscosity if it causes stresses to fall below the yield strength of the material. Because of this nonlinear feedback, mantle tractions can influence the strength of plate boundaries: Only when the stresses excited by the driving forces exceed the yield strength of the material, plate boundaries are weak and allow for plate-like motion. This explains why the reduction in driving forces causes a strong increase in angular misfit, which is not the case in more linear models. In addition, the strong impact of lower mantle heterogeneities compared to upper mantle slabs is likely related to a different balance between suction and slab pull force in their models. Apart from the use of a visco-elastic-plastic rheology, Osei Tutu, Sobolev, et al. (2018) also use a slightly higher asthenospheric viscosity than in our best-fit model, which allows tractions caused by slab suction to transmit higher stresses to the plates. More importantly, Osei Tutu, Sobolev, et al. (2018) do not include lateral viscosity variations below 300 km depth, and they employ an averaged tomography model (SMEAN, Becker & Boschi, 2002), which by nature features subducted slabs as broad structures. Consequently, slabs in their models cause a strong buoyancy force, but do not increase mantle viscosity, allowing them to sink faster and incite more mantle flow than in a model with temperature-dependent viscosity.

This phenomenon was already noted in Stadler et al. (2010), who found that plate velocities approximately double (their table S4, Figure S5) when temperature-dependence of viscosity in the lower mantle is neglected.

Our models improve on existing studies by including lateral viscosity variations in the lower mantle, and at the same time using the LLNL-G3D-JPS tomography model that features more clearly defined slab structures in the lower mantle compared to previous studies.

Our estimate on the amount of the slab pull force of $\leq$70% is consistent with Conrad and Lithgow-Bertelloni (2004), who find that slab pull provides 60-80% of the plate driving force, depending on the asthenosphere viscosity.

Our results also agree with the study of Conrad and Lithgow-Bertelloni (2002), who find that models with only slab suction still achieve a reasonable ($\sim$ 80%) angular correlation, but do not reproduce the observed relative speed between the different plates.

To estimate the balance of forces acting on the North American plate in particular, Liu and King (2022) test scenarios that either only include buoyancy from seismic tomography (in this case the S40RTS model) throughout the whole mantle, or, alternatively, replace fast seismic anomalies from 100 to 660 km depth by a global model of regionalized upper mantle slabs inferred from seismicity. They find that plate motions predicted from S40RTS alone are somewhat slower than in models that include slabs based on seismicity, but the directions generally fit observed plate motions well ($\xi = 0.858$). However, the direction of oceanic plates is predicted substantially better than that of the continental plates, with in particular the North American Plate moving in the opposite direction as observed. Based on these results, Liu and King (2022) argue that buoyancy derived from seismic tomography alone is not sufficient to predict the motion of continental plates in general and the North American plate in particular. Instead, they find the best fit to the North American plate motion when they remove the buoyancy below 660 km depth and additionally reduce the seismic-velocity-to-density scaling in seismically slow regions to account for the presence of partial melt.

This result is consistent with our model with laterally homogeneous buoyancy below 200 km (TM1_only), where the North American plate fits the observed velocity better than in our best-fit model both in direction and magnitude (Figure 11c). As in Liu and King (2022), our models also show a decrease in the general directional fit (from 91.5% to 74%) when only tomography-derived density anomalies are included, and only below 200 km depth (Figure 11a and d). However, a model setup closer to that of Liu and King (2022), where the transition from the TM1 model to tomography occurs at 100 km depth, features a similar angular fit as our reference model (91.6%; see Table 3). We attribute this good fit in our model even with seismic tomography alone to the better resolution of the LLNL-G3D-JPS compared to S40RTS used by Liu and King (2022), leading to coherent slabs in our models.

We note that all estimates for the relative percentage of forces have large uncertainties, because they depend on the asthenosphere and plate viscosities. The lower the asthenosphere viscosity, the bigger the effect of slab pull compared to suction (Conrad & Lithgow-Bertelloni, 2004). Our models show trade-offs between the two parameters, and they achieve a similar velocity residual for a range of parameter values. In addition, the force balance also depends on the scaling of seismic velocity to density, and on the lower mantle viscosity, since increased lower mantle viscosity increases the importance of slab pull over slab suction. However, our results in comparison to previous studies illustrate the importance of the coupling between upper-mantle and lower-mantle driving forces of plate tectonics. Particularly relevant seems to be the continuity of subducted slabs and their potential to act as stress guides, and the presence of lateral viscosity variations throughout the whole mantle.

Table 3. Misfit of various model configurations based on our reference case

Model name	Angular correlation (%)	Mean speed residual (cm/yr)	RMS velocity residual (cm/yr)
Reference model*	91.5	1.25	2.05
TM1 to LLNL-G3D-JPS transition at 300 km	87.27	1.50	2.65
TM1 to LLNL-G3D-JPS transition at 150 km	93.18	0.90	1.87
TM1 to LLNL-G3D-JPS transition at 100 km	91.6	1.39	2.67
TM1 model depths +30 km (see SI)	90.33	2.02	2.71
TM1 model depths −30 km (see SI)	51.27	13.9	29.04
Homogeneous tomography	79.8	2.05	3.18
Homogeneous sub-lithospheric mantle until 300 km	73.63	2.97	3.87
Increased craton strength	91.68	1.3	2.09
Increased slab strength	93.33	1.19	1.92
Grain size = 1.4 mm (see SI)	93.28	1.38	2.15
Constant Vs-to-T scaling (see SI)	91.5	1.17	2
Reference model (higher resolution)	90.6	1.38	2.16

*Reference model uses GEM plate boundaries, a plate boundary viscosity of 2.5×10^{20} Pa s and an asthenosphere viscosity of 5×10^{17} Pa s.

4 Conclusions

We have used instantaneous 3-D mantle convection simulations with a heterogeneous density and viscosity structure inferred from the LLNL-G3D-JPS tomography model to study the effects of plate driving and resisting forces on the observed surface deformation. In particular, we investigated the influence of varying friction at the plate boundaries and the base of the plates, different plate boundary geometries, and different upper-mantle viscosity structure defining slabs, cratons and the lithosphere. We find that both the frictional forces at plate boundaries and the base of plates and slab pull have a strong influence on the plate motions. In particular, plate boundaries that are 3 to 4 order of magnitude weaker than the surrounding lithosphere, and an intermediate to low asthenosphere viscosity of $5{\times}10^{17}$ to $5{\times}10^{18}$ Pa s lead to a reasonable fit to the observed GPS data both in terms of direction and speed of plate motion (Figure 5). Additionally, our models demonstrate that the choice of plate boundary geometry is critical for the direction of plate motions and affects which plates fit the observations well. Specifically, models based on the GEM database with open plate boundaries, dipping discrete (lithospheric depth) weak zones in the oceans and more diffused (crustal depth) weak zones within the continents achieve the lowest overall RMS velocity residuals relative to the observations (Figure 6). Our models also reaffirm the importance of slab pull for plate tectonics, showing that slab pull in the uppermost mantle (at depths <300 km) contributes more than half of the observed speed of plate motions (Figure 11), and that it is crucial for slabs to be connected to be able to transfer forces to the plate. Models without slab pull can only explain about 30% of the average plate speed. Using different temperature models for the lithosphere/upper mantle and the lower mantle (e.g. based on tomography) can easily lead to gaps in the slab structure, reducing the amount of slab pull being transferred to the plate.

The improved fit of the GEM models compared to models with closed plate boundaries (Figure 6) suggests two important physical properties of the plate boundaries on

Earth that should be considered in global mantle convection models: First, plate boundaries are not uniformly weak everywhere, and they do not have to be closed polygons. They are better described by using discrete, weak zones cutting through the whole lithosphere only in the oceanic regions, and instead a network of intra-plate faults down to the depth defined by seismicity in the continents, leading to plate boundaries that are not as weak as in the oceans and consequently more distributed deformation. Variable plate boundary viscosities have also been included in previous modeling studies to improve the plate motion fits regionally (Stadler et al., 2010; Alisic et al., 2012) or globally (Ghosh & Holt, 2012). However, the variability in the strength of plate boundaries is either based on observed strain rates (Ghosh & Holt, 2012), which is already a result of the deformation produced due to plate-driving forces and does not provide a physical explanation for why the strength varies, or is only included at one plate boundary (between the Nazca and South America in Stadler et al. (2010); Alisic et al. (2012)'s models). Second, it is important to include the dip angle of plate boundaries—as in the GEM-based models—rather than using vertical shear zones. This allows the slab pull forces to be transferred more efficiently to the subducting plate at the surface because the shear zones follow along the upper boundary of the subducting plate rather than cutting though it, and the deformation between the plates occurs at an angle that allows horizontal stresses to be transferred more easily.

Acknowledgements

We thank Anthony Osei Tutu for providing the TM1 temperature model used in this study, and the authors of LLNL-G3D-JPS tomography model for making their model publicly available. We would also like to thank Wolfgang Bangerth, John Naliboff, Shangxin Liu and Anthony Osei Tutu for insightful discussions and feedback on this study.

We thank the Computational Infrastructure for Geodynamics (geodynamics.org) which is funded by the National Science Foundation under award EAR-0949446 and EAR-1550901 for supporting the development of ASPECT. AS, RG and JD were supported by the NSF grant EAR-1925677.

This work used the Extreme Science and Engineering Discovery Environment (XSEDE), which is supported by National Science Foundation grant number ACI-1548562. Compute time was provided by CIG on the NSF-funded cluster EXPANSE, operated by the San Diego Supercomputer Center at UC San Diego. The authors acknowledge the Texas Advanced Computing Center (TACC, http://www.tacc.utexas.edu) at The University of Texas at Austin for providing high-performance computing resources on Frontera (Stanzione et al., 2020) that have contributed to the research results reported within this paper. The authors also acknowledge University of Florida Research Computing (https://www.rc.ufl.edu/) for providing additional computational resources and support that have contributed to the research results reported in this publication.

5 Data Availability

All models presented in the study are run using ASPECT version 2.4.0-pre (commit 7ee6c0ec6), which is freely available on Github (Kronbichler et al., 2012; Heister et al., 2017; Bangerth et al., 2022b, 2022a), compiled with the deal.II version 9.4.0. We use the branch `https://github.com/alarshi/WorldBuilder/tree/rounded_fault` in World builder to incorporate smooth viscosity transition from fault viscosity to lithospheric viscosity. We provide our material model plugin and all data necessary to reproduce our results as a data publication on Zenodo (Saxena et al., 2022).

References

Alisic, L., Gurnis, M., Stadler, G., Burstedde, C., & Ghattas, O. (2012). Multi-scale dynamics and rheology of mantle flow with plates. *Journal of Geophysical Research: Solid Earth*, *117*(B10).

Alisic, L., Gurnis, M., Stadler, G., Burstedde, C., Wilcox, L. C., & Ghattas, O. (2010). Slab stress and strain rate as constraints on global mantle flow. *Geophysical Research Letters*, *37*(22).

Arndt, D., Bangerth, W., Blais, B., Fehling, M., Gassmöller, R., Heister, T., ... others (2021). The deal. ii library, version 9.3. *Journal of Numerical Mathematics*, *29*(3), 171–186.

Artemieva, I. M. (2006). Global 1× 1 thermal model tc1 for the continental lithosphere: implications for lithosphere secular evolution. *Tectonophysics*, *416*(1-4), 245–277.

Balázs, A., Matenco, L., Vogt, K., Cloetingh, S., & Gerya, T. (2018). Extensional polarity change in continental rifts: Inferences from 3-d numerical modeling and observations. *Journal of Geophysical Research: Solid Earth*, *123*(9), 8073–8094.

Bangerth, W., Dannberg, J., Fraters, M., Gassmoeller, R., Glerum, A., Heister, T., ... Naliboff, J. (2022a, July). ASPECT*: Advanced Solver for Problems in Earth's ConvecTion, User Manual.* (doi:10.6084/m9.figshare.4865333) doi: 10.6084/m9.figshare.4865333

Bangerth, W., Dannberg, J., Fraters, M., Gassmoeller, R., Glerum, A., Heister, T., ... Naliboff, J. (2022b, July). *Aspect v2.4.0.* Zenodo. doi: 10.5281/zenodo.6903424

Becker, T. W. (2006). On the effect of temperature and strain-rate dependent viscosity on global mantle flow, net rotation, and plate-driving forces. *Geophysical Journal International*, *167*(2), 943–957.

Becker, T. W., & Boschi, L. (2002). A comparison of tomographic and geodynamic mantle models. *Geochemistry, Geophysics, Geosystems*, *3*(1).

Becker, T. W., & O'Connell, R. J. (2001). Predicting plate velocities with mantle circulation models. *Geochemistry, Geophysics, Geosystems*, *2*(12).

Billen, M. I., & Hirth, G. (2007). Rheologic controls on slab dynamics. *Geochemistry, Geophysics, Geosystems*, *8*(8).

Bird, P. (2003). An updated digital model of plate boundaries. *Geochemistry, Geophysics, Geosystems*, *4*(3).

Braun, J., Burbidge, D., Gesto, F., Sandiford, M., Gleadow, A. J. W., Kohn, B., & Cummins, P. (2009). Constraints on the current rate of deformation and surface uplift of the australian continent from a new seismic database and low-t thermochronological data. *Australian Journal of Earth Sciences*, *56*(2), 99–110.

Burstedde, C., Wilcox, L. C., & Ghattas, O. (2011). p4est: Scalable algorithms for parallel adaptive mesh refinement on forests of octrees. *SIAM Journal on Scientific Computing*, *33*(3), 1103–1133.

Calais, E., & Stein, S. (2009). Time-variable deformation in the new madrid seismic zone. *Science*, *323*(5920), 1442–1442.

Capitanio, F. A., Morra, G., & Goes, S. (2009). Dynamics of plate bending at the trench and slab-plate coupling. *Geochemistry, Geophysics, Geosystems*, *10*(4).

Clevenger, T. C., & Heister, T. (2021, March). Comparison between algebraic and matrix-free geometric multigrid for a Stokes problem on an adaptive mesh with variable viscosity. *Numerical Linear Algebra with Applications*. doi: 10.1002/nla.2375

Conrad, C. P., Bilek, S., & Lithgow-Bertelloni, C. (2004). Great earthquakes and slab pull: interaction between seismic coupling and plate–slab coupling. *Earth and Planetary Science Letters*, *218*(1-2), 109–122.

Conrad, C. P., & Lithgow-Bertelloni, C. (2002). How mantle slabs drive plate tectonics. *Science*, *298*(5591), 207–209.
Conrad, C. P., & Lithgow-Bertelloni, C. (2004). The temporal evolution of plate driving forces: Importance of "slab suction" versus "slab pull" during the cenozoic. *Journal of Geophysical Research: Solid Earth*, *109*(B10).
Conrad, C. P., & Lithgow-Bertelloni, C. (2006). Influence of continental roots and asthenosphere on plate-mantle coupling. *Geophysical Research Letters*, *33*(5).
DeMets, C., Gordon, R. G., Argus, D., & Stein, S. (1990). Current plate motions. *Geophysical journal international*, *101*(2), 425–478.
Forsyth, D., & Uyeda, S. (1975). On the relative importance of the driving forces of plate motion. *Geophysical Journal International*, *43*(1), 163–200.
Fraters, M. (2021, June). *The geodynamic world builder.* Zenodo. doi: 10.5281/zenodo.5014808
Fraters, M., Thieulot, C., van den Berg, A., & Spakman, W. (2019). The geodynamic world builder: a solution for complex initial conditions in numerical modeling. *Solid Earth*, *10*(5), 1785–1807. doi: 10.5194/se-10-1785-2019
Ghosh, A., Becker, T., & Humphreys, E. (2013). Dynamics of the north american continent. *Geophysical Journal International*, *194*(2), 651–669.
Ghosh, A., & Holt, W. E. (2012). Plate motions and stresses from global dynamic models. *Science*, *335*(6070), 838–843.
Gordon, R. G. (1998). The plate tectonic approximation: Plate nonrigidity, diffuse plate boundaries, and global plate reconstructions. *Annual Review of Earth and Planetary Sciences*, *26*(1), 615–642.
Heister, T., Dannberg, J., Gassmöller, R., & Bangerth, W. (2017). High accuracy mantle convection simulation through modern numerical methods–ii: realistic models and problems. *Geophysical Journal International*, *210*(2), 833–851.
Jarvis, G. T., & Mckenzie, D. P. (1980). Convection in a compressible fluid with infinite prandtl number. *Journal of Fluid Mechanics*, *96*(3), 515–583.
Kreemer, C., Blewitt, G., & Klein, E. C. (2014). A geodetic plate motion and global strain rate model. *Geochemistry, Geophysics, Geosystems*, *15*(10), 3849–3889.
Kreemer, C., & Holt, W. E. (2001). A no-net-rotation model of present-day surface motions. *Geophysical Research Letters*, *28*(23), 4407–4410.
Kronbichler, M., Heister, T., & Bangerth, W. (2012). High accuracy mantle convection simulation through modern numerical methods. *Geophysical Journal International*, *191*, 12-29. doi: 10.1111/j.1365-246X.2012.05609.x
Laske, G., Masters, G., Ma, Z., & Pasyanos, M. (2012). Crust1. 0: An updated global model of earth's crust. *Geophys Res Abs*, *14*, 3743.
Li, C., van der Hilst, R. D., Engdahl, E. R., & Burdick, S. (2008). A new global model for p wave speed variations in earth's mantle. *Geochemistry, Geophysics, Geosystems*, *9*(5).
Liu, S., & King, S. D. (2019). A benchmark study of incompressible stokes flow in a 3-d spherical shell using aspect. *Geophysical Journal International*, *217*(1), 650–667.
Liu, S., & King, S. D. (2022). Dynamics of the north american plate: Large-scale driving mechanism from far-field slabs and the interpretation of shallow negative seismic anomalies. *Geochemistry, Geophysics, Geosystems*, *23*(3), e2021GC009808.
Müller, R. D., Sdrolias, M., Gaina, C., & Roest, W. R. (2008). Age, spreading rates, and spreading asymmetry of the world's ocean crust. *Geochemistry, Geophysics, Geosystems*, *9*(4).
Nataf, H.-C., & Ricard, Y. (1996). 3smac: an a priori tomographic model of the upper mantle based on geophysical modeling. *Physics of the Earth and Planetary Interiors*, *95*(1-2), 101–122.
Osei Tutu, A., Sobolev, S. V., Steinberger, B., Popov, A. A., & Rogozhina, I. (2018). Evaluating the influence of plate boundary friction and mantle viscosity on

plate velocities. *Geochemistry, Geophysics, Geosystems*, *19*(3), 642–666.

Osei Tutu, A., Steinberger, B., Sobolev, S. V., Rogozhina, I., & Popov, A. A. (2018). Effects of upper mantle heterogeneities on the lithospheric stress field and dynamic topography. *Solid Earth*, *9*(3), 649–668.

Pagani, M., Garcia-Pelaez, J., Gee, R., Johnson, K., Poggi, V., Styron, R., … Monelli, D. (2018). Global earthquake model (gem) seismic hazard map (version 2018.1 - december 2018). *Creative Commons Attribution-NonCommercial-ShareAlike 4.0 International License (CC BY-NC-SA).*

Priestley, K., McKenzie, D., & Ho, T. (2018). A lithosphere–asthenosphere boundary—a global model derived from multimode surface-wave tomography and petrology. *Lithospheric discontinuities*, 111–123.

Ritsema, J., Deuss, A., Van Heijst, H., & Woodhouse, J. (2011). S40rts: a degree-40 shear-velocity model for the mantle from new rayleigh wave dispersion, teleseismic traveltime and normal-mode splitting function measurements. *Geophysical Journal International*, *184*(3), 1223–1236.

Ritsema, J., & Van Heijst, H. J. (2000). Seismic imaging of structural heterogeneity in earth's mantle: evidence for large-scale mantle flow. *Science Progress (1933-)*, 243–259.

Rolf, T., & Tackley, P. (2011). Focussing of stress by continents in 3d spherical mantle convection with self-consistent plate tectonics. *Geophysical Research Letters*, *38*(18).

Saxena, A., Dannberg, J., & Gassmoeller, R. (2022, October). *Dataset for High-resolution mantle flow models reveal importance of plate boundary geometry and slab pull forces on generating tectonic plate motions.* Zenodo. Retrieved from `https://doi.org/10.5281/zenodo.7225629` doi: 10.5281/zenodo.7225629

Schubert, G., Turcotte, D. L., & Olson, P. (2001). *Mantle convection in the earth and planets.* Cambridge University Press.

Simmons, N. A., Myers, S., Johannesson, G., Matzel, E., & Grand, S. (2015). Evidence for long-lived subduction of an ancient tectonic plate beneath the southern indian ocean. *Geophysical Research Letters*, *42*(21), 9270–9278.

Simmons, N. A., Myers, S. C., Johannesson, G., & Matzel, E. (2012). Llnl-g3dv3: Global p wave tomography model for improved regional and teleseismic travel time prediction. *Journal of Geophysical Research: Solid Earth*, *117*(B10).

Simmons, N. A., Schuberth, B. S., Myers, S. C., & Knapp, D. R. (2019). Resolution and covariance of the llnl-g3d-jps global seismic tomography model: applications to travel time uncertainty and tomographic filtering of geodynamic models. *Geophysical Journal International*, *217*(3), 1543–1557.

Stadler, G., Gurnis, M., Burstedde, C., Wilcox, L. C., Alisic, L., & Ghattas, O. (2010). The dynamics of plate tectonics and mantle flow: From local to global scales. *Science*, *329*(5995), 1033–1038.

Stanzione, D., West, J., Evans, R. T., Minyard, T., Ghattas, O., & Panda, D. K. (2020). Frontera: The evolution of leadership computing at the national science foundation. In *Practice and experience in advanced research computing* (pp. 106–111).

Steinberger, B. (2000). Slabs in the lower mantle—results of dynamic modelling compared with tomographic images and the geoid. *Physics of the Earth and Planetary Interiors*, *118*(3-4), 241–257.

Steinberger, B., & Calderwood, A. R. (2006). Models of large-scale viscous flow in the earth's mantle with constraints from mineral physics and surface observations. *Geophysical Journal International*, *167*(3), 1461–1481.

Styron, R., & Pagani, M. (2020). The gem global active faults database. *Earthquake Spectra*, *36*.

Van Wijk, J. (2005). Role of weak zone orientation in continental lithosphere extension. *Geophysical Research Letters*, *32*(2).

Wu, B., Conrad, C. P., Heuret, A., Lithgow-Bertelloni, C., & Lallemand, S. (2008). Reconciling strong slab pull and weak plate bending: The plate motion constraint on the strength of mantle slabs. *Earth and Planetary Science Letters*, *272*(1-2), 412–421.
Zhong, S. (2001). Role of ocean-continent contrast and continental keels on plate motion, net rotation of lithosphere, and the geoid. *Journal of Geophysical Research: Solid Earth*, *106*(B1), 703–712.
Zhong, S., Gurnis, M., & Moresi, L. (1998). Role of faults, nonlinear rheology, and viscosity structure in generating plates from instantaneous mantle flow models. *Journal of Geophysical Research: Solid Earth*, *103*(B7), 15255–15268.
Zoback, M. D., Townend, J., & Grollimund, B. (2002). Steady-state failure equilibrium and deformation of intraplate lithosphere. *International Geology Review*, *44*(5), 383–401.

Supporting Information for "High-resolution mantle flow models reveal importance of plate boundary geometry and slab pull forces on generating tectonic plate motions"

A. Saxena[1], J. Dannberg[1], R. Gassmöller[1], M. Fraters[2], T. Heister[3], and R. Styron[4]

[1]Department of Geological Sciences, University of Florida, Gainesville, FL, USA

[2]Department of Earth and Planetary Sciences, University of California, Davis, CA, USA

[3]Mathematical and Statistical Sciences, Clemson University, Clemson, SC, USA

[4]Global Earthquake Model Foundation, Pavia, Italy

Contents of this file

Introduction Our main text describes our global mantle flow model setup and presents results from our parameter study with varying plate boundary and asthenosphere viscosities and different plate boundary configurations, testing which model best fits the observed plate motions. Here we describe additional parameter variations based on our best-fit model, i.e., the model with the GEM plate geometry, an asthenosphere viscosity of 5×10^{17} Pa s and a plate boundary viscosity of 2.5×10^{20} Pa s.

Influence of temperature distribution

To account for uncertainties in lithosphere thickness, we test models with a thicker and a thinner lithosphere by shifting the TM1 temperature model (Osei Tutu et al., 2018) we use as an input upwards and downwards by 30 km, respectively. In the model with a thinner lithosphere, the plates move very fast (average rms velocity ∼14 cm/yr) compared to the average GPS velocities. This is expected because shifting the temperature structure up by 30 km leads to higher temperatures of the lithospheric mantle and consequently low-viscosity thin plates that can deform very easily. The angular fits deteriorate from 91.5% in our reference case to ≈50% in this model. Increased plate speeds in models with a thinner lithosphere were also reported by Osei Tutu et al. (2018). However, the increase in speed and angular misfit is much higher in our model due to the absence of a rigid crust in some parts of the model.

The model with a thicker lithosphere (Figure S6) has a similar angular correlation, but a higher speed residual (2.02 versus 1.25 cm/yr) and RMS residual (2.71 vs 2.05 cm/yr) compared to our reference model. The reason for this higher speed residual is an overall reduction in the speed of the plates, particularly in the oceanic plates, because the same forces are transferred to a thicker plate—an effect also observed in Osei Tutu et al. (2018)'s models. While this results in an increased speed residual for most oceanic plates (e.g., Pacific, Australia and Cocos), the reduced speed fits the observed motion of the Nazca plate better compared to the reference model, where the velocities are too high (Fig. S6, Fig. 7).

Our tests with the shifted TM1 model shows that lithospheric structure strongly affects the plate speeds and directions, and future improvements in lithospheric thickness estimates could improve the fit to the observations.

We also test a constant Vs-to-temperature anomaly scaling (Vs-to-T) factor of -4.2 (as in Becker, 2006) instead of the depth-dependent scaling used in our other models (from Steinberger & Calderwood, 2006). We find that our results remain largely unaffected with slightly higher velocities (average speeds are 5% more than our reference model) predicted with the constant Vs-to-T factor. This is because compared to the depth-dependent Vs-to-T values used in our other models, the constant Vs-to-T factor is larger at shallower depths (<250 km) and smaller below 250 km depth. A higher Vs-to-T scaling implies stronger temperature variations and a stronger associated buoyancy force. The increased uppermost-mantle temperature variations in the models with a constant scaling (compared to the model with depth-dependent scaling) influence the plate velocities more than the decreased lower-mantle temperature variations. The higher contribution of upper-mantle heterogeneity compared to the lower-mantle is consistent with our analysis of the forces contributing to plate motion discussed in Section 3.6 of the main text.

Influence of grain size

In our best-fit model, we modify the slab strength by shifting the ratio between diffusion and dislocation creep. We achieve this by reducing the grain size from 5 mm in the reference model to 1.4 mm, reducing the viscosity in regions where diffusion creep contributes to deformation. The viscosity in regions with strong deformation, such as subducted slabs, that are dominated by dislocation creep are not affected by grain size. This increases the relative viscosity contrast between subducted slabs and the rest of the mantle. Since we scale the laterally averaged viscosity to a reference profile (see Section 2.5), changing the grain size in this way does not affect the average viscosity values, but it does lead to higher viscosities in slabs. This means that slab pull forces can now be transferred more efficiently to the plates attached to the subduction zone. Our model with reduced grain size has an improved angular correlation of 93.3% (compared to 91.5% in the reference model) and a slightly increased mean speed residual (1.4 cm/yr vs 1.25 cm/yr) with the overall effect of a marginally increased velocity residual (2.15 cm/yr from 2.05 cm/yr). In the Earth, grain size is expected to vary based on the temperature and deformation conditions, affecting the spatial variability of viscosity and therefore the mantle flow pattern (Dannberg et al., 2017). This more complex effect remains to be investigated in future studies.

References

Argus, D. F., & Gordon, R. G. (1991). No-net-rotation model of current plate velocities incorporating plate motion model nuvel-1. *Geophysical research letters*, *18*(11), 2039–2042.

Becker, T. W. (2006). On the effect of temperature and strain-rate dependent viscosity on global mantle flow, net rotation, and plate-driving forces. *Geophysical Journal International*, *167*(2), 943–957.

Bird, P. (2003). An updated digital model of plate boundaries. *Geochemistry, Geophysics, Geosystems*, *4*(3).

Dannberg, J., Eilon, Z., Faul, U., Gassmöller, R., Moulik, P., & Myhill, R. (2017). The importance of grain size to mantle dynamics and seismological observations. *Geochemistry, Geophysics, Geosystems*, *18*(8), 3034–3061.

Osei Tutu, A., Steinberger, B., Sobolev, S. V., Rogozhina, I., & Popov, A. A. (2018). Effects of upper mantle heterogeneities on the lithospheric stress field and dynamic topography. *Solid Earth*, *9*(3), 649–668.

Simmons, N. A., Myers, S., Johannesson, G., Matzel, E., & Grand, S. (2015). Evidence for long-lived subduction of an ancient tectonic plate beneath the southern indian ocean. *Geophysical Research Letters*, *42*(21), 9270–9278.

Steinberger, B., & Calderwood, A. R. (2006). Models of large-scale viscous flow in the earth's mantle with constraints from mineral physics and surface observations. *Geophysical Journal International*, *167*(3), 1461–1481.

Styron, R., & Pagani, M. (2020). The gem global active faults database. *Earthquake Spectra*, *36*.

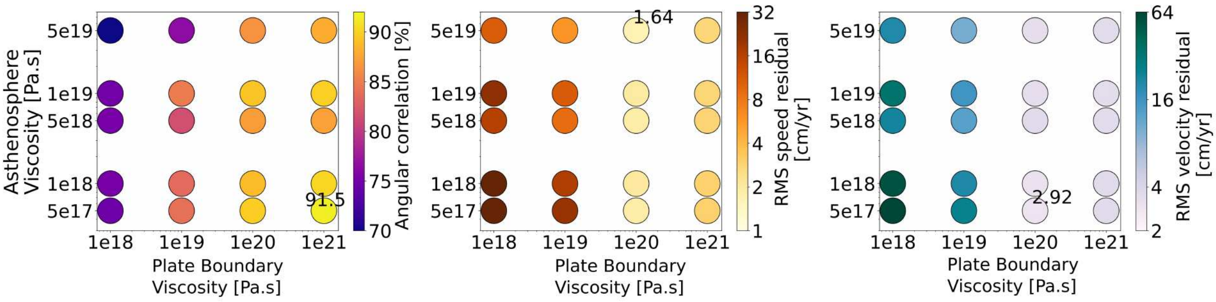

Figure S1. Angular correlation, mean speed residuals and velocity residuals at the surface for the models shown in Figure 4 in the main text (Bird-closed plate geometry, and using different values of plate boundary viscosity and asthenosphere viscosity). Maximum angular correlation, minimum speed residual, and minimum velocity residual are annotated in each subplot. Note that in all plots light colors represent a good fit, and saturated colors represent significant misfits.

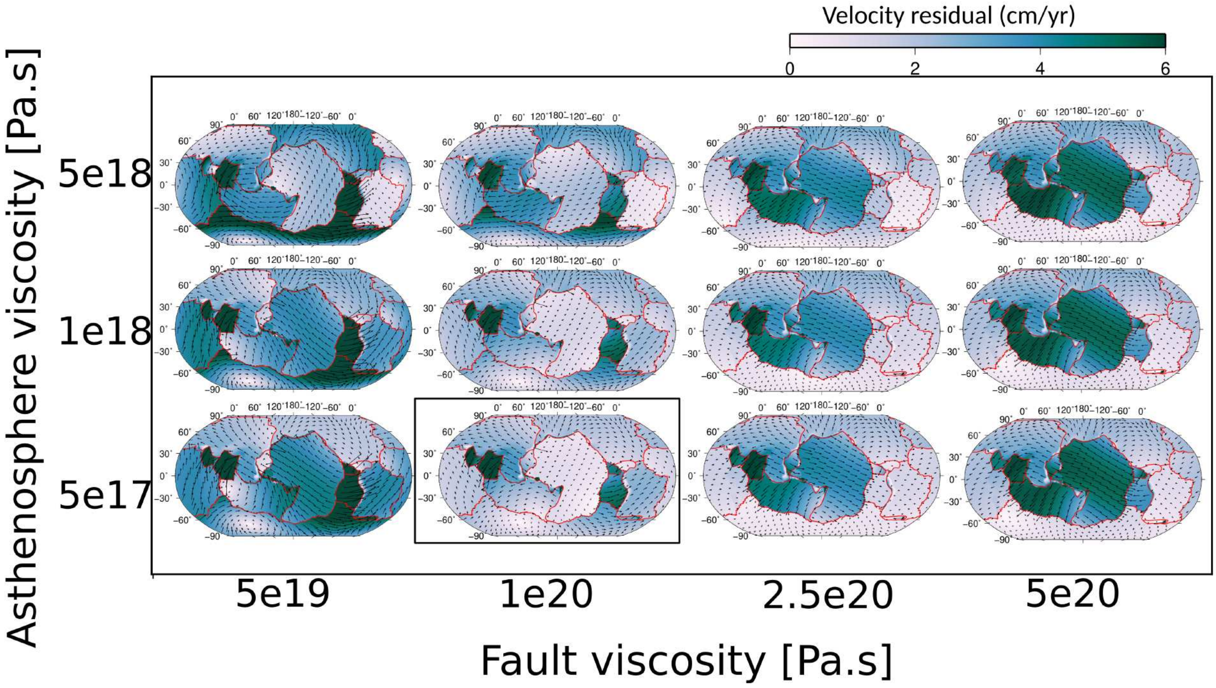

Figure S2. Velocity residual at the surface for different combinations of plate boundary viscosity and asthenosphere viscosity (as in Figure 5 in the main text), and using the Nuvel plate boundary geometry (Argus & Gordon, 1991). The arrows represent point-wise differences between modeled and observed velocity vectors. The black box marks the models with the lowest RMS velocity residual.

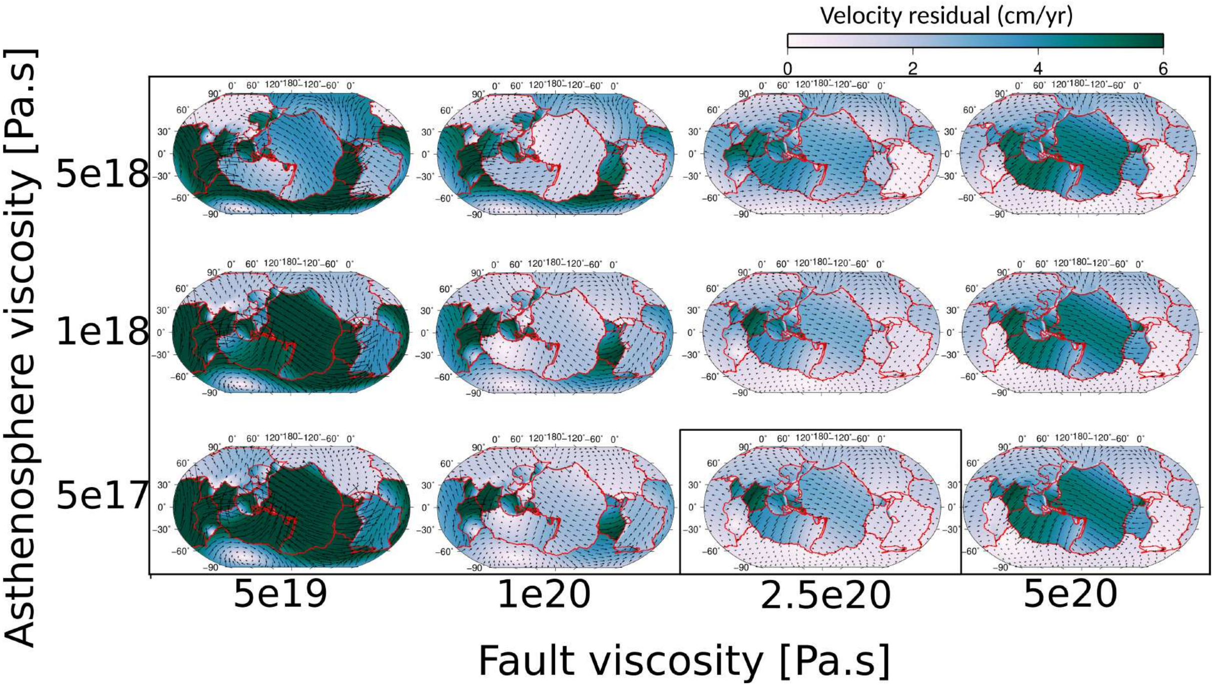

Figure S3. Velocity residual at the surface for different combinations of plate boundary viscosity and asthenosphere viscosity (as in Figure 5 in the main text), and using the Bird-closed plate boundary geometry (Bird, 2003). The arrows represent point-wise differences between modeled and observed velocity vectors. The black box marks the models with the lowest RMS velocity residual.

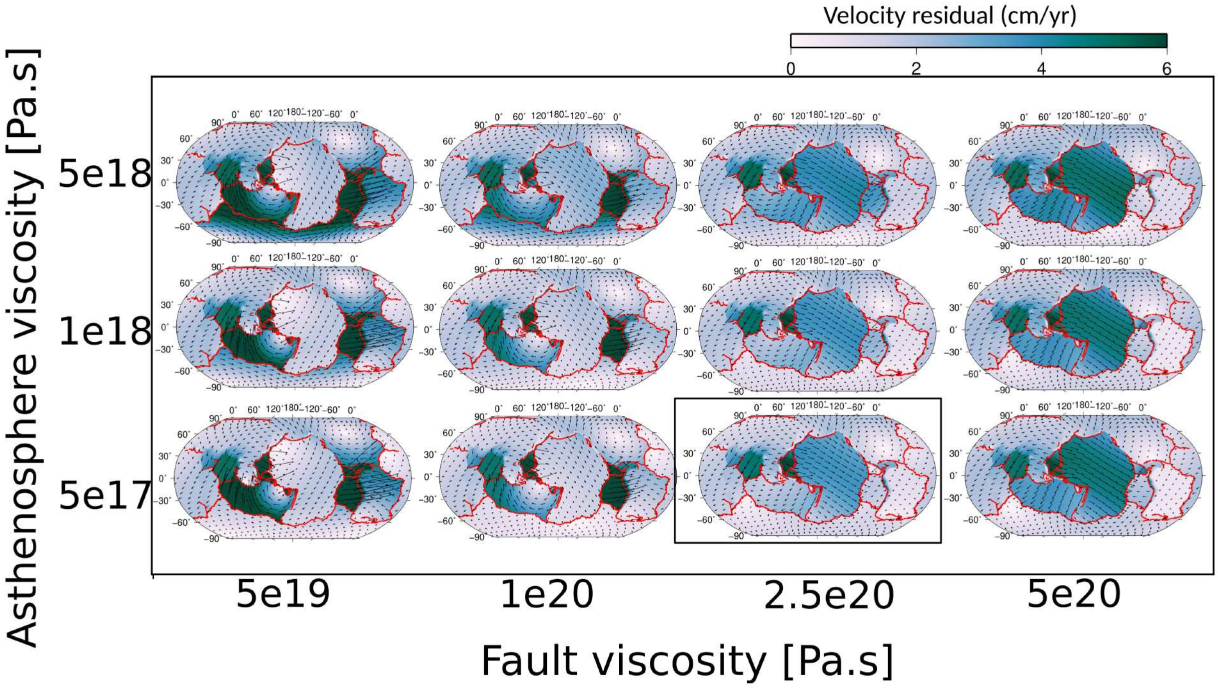

Figure S4. Velocity residual at the surface for different combinations of plate boundary viscosity and asthenosphere viscosity (as in Figure 5 in the main text), and using the Bird-GEM plate boundary geometry (Bird, 2003; Styron & Pagani, 2020). The arrows represent point-wise differences between modeled and observed velocity vectors. The black box marks the models with the lowest RMS velocity residual.

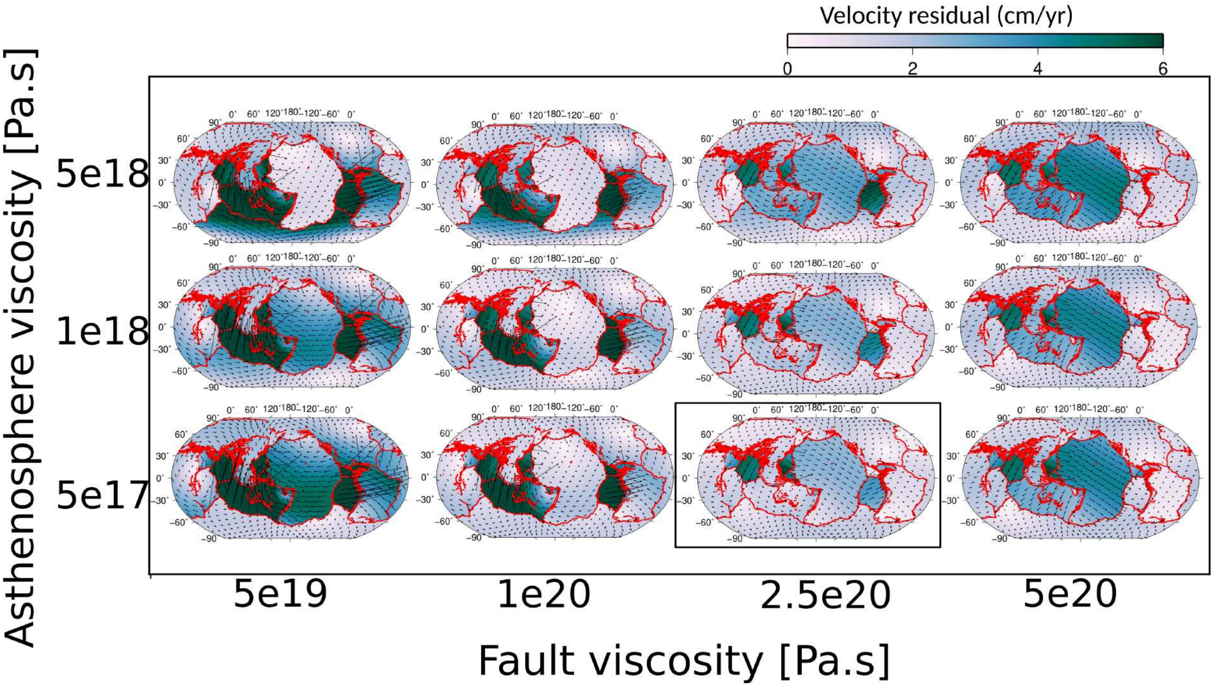

Figure S5. Velocity residual at the surface for different combinations of plate boundary viscosity and asthenosphere viscosity (as in Figure 5 in the main text), and using the GEM plate boundary geometry (Styron & Pagani, 2020). The arrows represent point-wise differences between modeled and observed velocity vectors. The black box marks the models with the lowest RMS velocity residual.

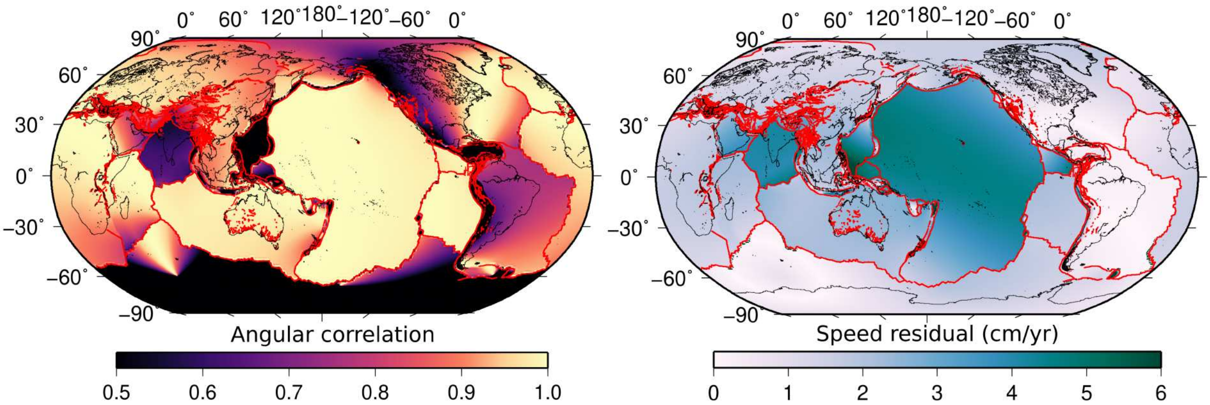

Figure S6. Map of angular correlation and speed residual for the model with a thicker lithosphere.

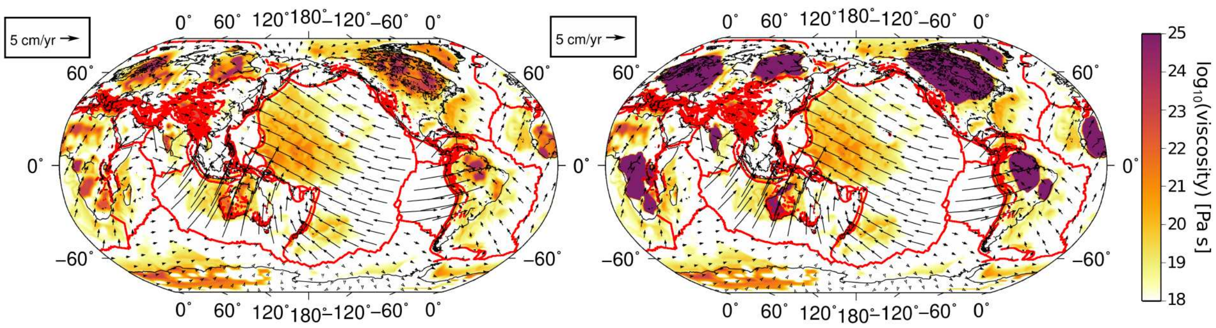

Figure S7. Viscosity at 100 km depth for our reference model (left) and model with stiff cratons (right). The modeled and observed surface velocities for the corresponding models are shown using black arrows, respectively.

Table S1. Velocity residuals of models with different transition depths between the TM1 temperature model (Osei Tutu et al., 2018) and the LLNL tomography model (Simmons et al., 2015)

Plate boundary model	Plate boundary viscosity	Asthenosphere viscosity	TM1 to LLNL transition depth (km)	Mean velocity residual (cm/yr)
Bird-closed	1e20	1e18	100	7.89
Bird-closed	1e20	1e18	150	4.71
Bird-closed	1e20	1e18	200	3.21
Bird-closed	1e20	1e18	300	3.3
Bird-GEM	1e20	1e18	150	3.58
Bird-GEM	1e20	1e18	200	3.22
Bird-GEM	1e20	1e18	300	3.48

Table S2. Misfit of various model configurations with varying plate boundary and asthenosphere viscosity, and plate boundary models

Plate boundary model	Plate boundary viscosity	Asthenosphere viscosity	Angular correlation (%)	Mean speed residual (cm/yr)	Mean velocity residual (cm/yr)
Nuvel	5e20	5e18	80.7	2.62	3.38
Nuvel	5e20	1e18	82.51	2.7	3.38
Nuvel	5e20	5e17	86.27	2.75	3.384
Nuvel	2.5e20	5e18	81.06	2.07	2.94
Nuvel	2.5e20	1e18	82.55	2.05	2.82
Nuvel	2.5e20	5e17	85.93	2.07	2.8
Nuvel	1e20	5e18	81.71	1.71	2.93
Nuvel	1e20	1e18	83.61	1.46	2.65
Nuvel	1e20	5e17	85.9	1.34	2.52
Nuvel	5e19	5e18	82.08	2.32	4.14
Nuvel	5e19	1e18	84.76	3	4.56
Nuvel	5e19	5e17	86.25	3.07	4.68
Bird-closed	5e20	5e18	87.52	2.33	3.1
Bird-closed	5e20	1e18	90.2	2.38	3.03
Bird-closed	5e20	5e17	91.21	2.44	3.05
Bird-closed	2.5e20	5e18	87.52	1.85	2.7
Bird-closed	2.5e20	1e18	89.76	1.67	2.34
Bird-closed	2.5e20	5e17	90.72	1.61	2.28
Bird-closed	1e20	5e18	87.08	1.91	3.58
Bird-closed	1e20	1e18	88.9	2.04	3.12
Bird-closed	1e20	5e17	89.78	1.91	2.92
Bird-closed	5e19	5e18	86.23	3.6	5.75
Bird-closed	5e19	1e18	88.05	4.7	6.41
Bird-closed	5e19	5e17	88.74	4.93	6.6
Bird-gem	5e20	5e18	90.4	2.35	3.01
Bird-gem	5e20	1e18	91.68	2.32	2.9
Bird-gem	5e20	5e17	91.87	2.31	2.87
Bird-gem	2.5e20	5e18	89.4	2.06	2.73
Bird-gem	2.5e20	1e18	90.88	1.8	2.44
Bird-gem	2.5e20	5e17	91.21	1.74	2.37
Bird-gem	1e20	5e18	87.34	2.25	3.48
Bird-gem	1e20	1e18	89.82	1.85	3.22
Bird-gem	1e20	5e17	89.4	1.71	3.06
Bird-gem	5e19	5e18	85.5	2.81	5.13
Bird-gem	5e19	1e18	86.6	2.7	5.67
Bird-gem	5e19	5e17	86.9	2.61	5.64
GEM	5e20	5e18	90.88	2.04	2.77
GEM	5e20	1e18	93.01	2	2.61
GEM	5e20	5e17	92.67	2.01	2.6
GEM	2.5e20	5e18	90.06	1.65	2.56
GEM	2.5e20	1e18	92.1	1.33	2.15
GEM	2.5e20	5e17	91.5	1.25	2.05
GEM	1e20	5e18	88.15	1.96	3.96
GEM	1e20	1e18	89.92	1.79	4.05
GEM	1e20	5e17	89.24	1.87	4
GEM	5e19	5e18	86.32	2.85	6.12
GEM	5e19	1e18	87.57	3.83	7.66
GEM	5e19	5e17	87	4.21	8